Narrowband biphoton generation in the group delay regime

Luwei Zhao, Yumian Su,* and Shengwang Du†
Department of Physics, The Hong Kong University of Science and Technology, Clear Water Bay, Kowloon, Hong Kong, China
(Received 16 December 2015; published 9 March 2016)

We study narrowband biphoton generation from spontaneous four-wave mixing with electromagnetically induced transparency in a laser-cooled atomic ensemble. We compare two formalisms in the interaction and Heisenberg pictures and find that they agree in the low-gain regime but disagree in the high-gain regime. We extend both formalisms to account for the nonuniformity of the atomic density and the driving laser fields. We find that for a fixed optical depth and a weak and far-detuned pump laser beam, the two-photon waveform is independent of the atomic density distribution. However, the spatial profiles of the two driving laser beams have significant effects on the biphoton temporal waveform. We predict that waveform shaping in the time domain can be achieved by controlling the spatial profiles of the driving laser fields.

DOI: 10.1103/PhysRevA.93.033815

I. INTRODUCTION

Entangled photon pairs, termed biphotons, have been studied extensively for a range of quantum applications, including quantum information processing, quantum communication, and quantum cryptography [1,2]. To improve its spectral brightness, a lot of efforts have been made to generate narrowband, long coherent biphotons using various methods, e.g., cavity-assisted spontaneous parametric down conversion (SPDC) in nonlinear crystals [3–7] and spontaneous four-wave mixing (SFWM) in atomic systems [8–12]. These biphotons can be used to produce narrow-band heralded single photons, as the time origin is established by one of the paired photons. With the long coherence time ranging from several hundred nanoseconds to microseconds, the heralded single-photon waveform can be shaped by an electro-optical modulator [13]. Their ability to interact with atoms resonantly has found applications in observing single-photon optical precursors [14], improving the storage efficiency of optical quantum memory [15], and coherently controlling absorption and reemission of single photons in two-level atoms [16]. Other applications include single-photon differential-phase-shift quantum key distribution [17]. However, external amplitude modulation causes unavoidable loss to the single photons and also introduces noise. The ideal way to create a desired biphoton waveform is to start from biphoton generation, i.e., to control the driving field and the medium. For the broadband entangled photons generated by SPDC, Valencia *et al.* [18] demonstrated shaping the joint spectrum by controlling the spatial shape of the pump beam, which is the first spatial-to-spectrum mapping of biphotons. For an SFWM narrowband biphoton source with electromagnetically induced transparency (EIT), the two-photon correlation function can be shaped by periodically modulating the classical driving fields in the time domain [19,20].

In the literature, there are two formalisms to model the EIT-assisted SFWM process. One uses the perturbation theory in the interaction picture, in which the interaction Hamiltonian describes the four-wave mixing process and determines the evolution of the two-photon state vector [21–25]. This gives a clear picture of the biphoton generation mechanism. The other is developed in the Heisenberg picture [26–29] with the evolution of field operators. In all these previous theoretical models, the atomic density and driving field amplitude are spatially uniform and thus the effect of their nonuniformity has not been studied.

Unlike the rectangle-shaped biphoton waveform predicted previously in the group delay regime [8,25,26], in our recent experiment [12] we produced a Gaussian-like biphoton waveform at a large atomic optical depth (OD). This shape cannot be explained by current theoretical models, and this is one of our motivations for extending the existing models.

In this paper, we explore the following points. (i) *Comparison of the two models*: We compare the two formalisms in the interaction and Heisenberg pictures and show that in the low-parametric-gain regime they agree well. (ii) *Nonuniformity*: We extend the existing theories by taking into account the nonuniformity in the atom distribution, the pump, and the coupling laser intensity distribution in the longitudinal direction of the atomic cloud. We show that the profiles of the pump and coupling laser intensities have significant effects on the biphoton waveform. (iii) *Waveform shaping*: By controlling the spatial profile of the driving field, we can shape the biphoton waveform in the time domain. On the other hand, the time-domain waveform of the photon pairs allows us to retrieve information on the spatial profile of the pump and coupling laser beams.

The paper is organized as follows: In Sec. II, we describe the biphoton generation using two approaches: (i) state vector theory in the interaction picture and (ii) coupled operator equations in the Heisenberg picture. Section III gives the numerical results of the models. We first analyze the photon properties, then show that the two approaches are equivalent in the low-parametric-gain regime. We then propose to shape and engineer biphoton temporal waveforms with various spatial profiles of the driving lasers in Sec. IV. We give our conclusions in Sec. V.

II. THEORETICAL FRAMEWORK

In this paper, we study EIT-assisted SFWM biphoton generation in both the interaction and the Heisenberg pictures.

*yumiansu@ust.hk
†dusw@ust.hk

Extending from previous models, we take into account the nonuniformity of the atomic density and the spatial profiles of the driving fields. Although both pictures are equivalent, some physics insights are clearer in one picture or the other. In the interaction picture, using perturbation theory, the evolution of the photon state describes more clearly how biphotons are generated, but the system loss and gain cannot be fully accounted for. On the other side, the Heisenberg formalism provides a more accurate calculation of the experimental coincidence counts including multiphoton events and accidental coincidences, but the two-photon state is not clearly resolved. We compare the two models by exploring the scenario in which the atomic density and the intensities of the pump and coupling lasers are not uniform along the length of the atomic cloud.

Figure 1 is a schematic of biphoton generation from a four-level double-Λ cold atomic medium of length L. The atoms are identical and prepared in the ground state $|1\rangle$. A pump laser with frequency ω_p excites the transition $|1\rangle \rightarrow |4\rangle$ with a detuning Δ_p, and a coupling laser on resonance with the transition $|2\rangle \rightarrow |3\rangle$ propagates in the opposite direction of the pump laser. Phase-matched, counter-propagating Stokes (ω_s) and anti-Stokes ($\omega_{\rm as}$) photon pairs are spontaneously generated following the SFWM path. The coupling laser renders the EIT window for the resonant anti-Stokes photons, which travel at a slow group velocity [30,31]. The Stokes photons travel in the atomic cloud nearly at the speed of light in vacuum and with a negligible Raman gain. The counter-propagating pump-coupling beams are aligned with a small angle θ with respect to the biphoton generation longitudinal z axis. Assuming that the pump laser is weak and far detuned from the $|1\rangle \rightarrow |4\rangle$ transition, the majority of the atoms are in the ground state $|1\rangle$.

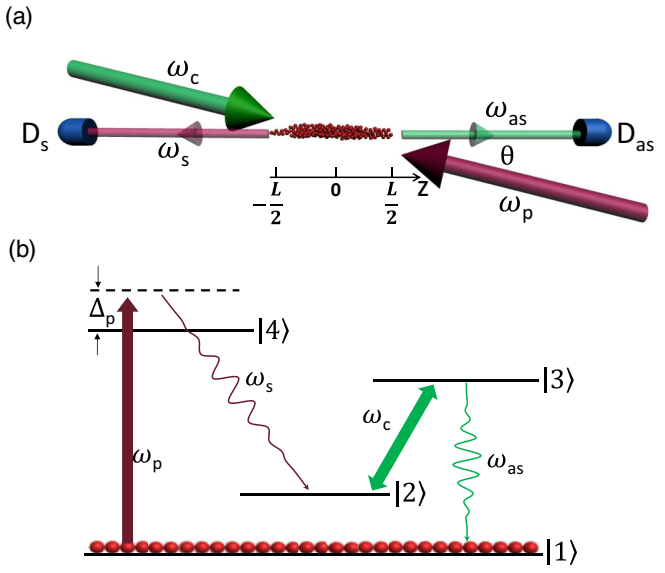

FIG. 1. Schematic of four-wave mixing to generate biphotons. (a) Optical configuration. (b) Atomic energy level diagram. The pump laser couples the transition $|1\rangle \rightarrow |4\rangle$ with a detuning Δ_p, while the coupling laser is on resonance with the transition $|2\rangle \rightarrow |3\rangle$. Paired Stokes and anti-Stokes photons are spontaneously produced following the SFWM path.

A. Interaction picture

Here we study biphoton generation in the interaction picture with a focus on the evolution of the two-photon state. We extend the previous theory of Du *et al.* [25] to take into account the spatial nonuniformity of the nonlinear interaction. With the z direction being the longitudinal direction of the biphoton generation as shown in Fig. 1, the electric field in this direction is given by $E(z,t) = [E^{(+)}(z,t) + E^{(-)}(z,t)]/2$, where $E^{(\pm)}$ are positive and negative frequency parts. Assuming that the counter-propagating pump and coupling laser beams are undepleted in the atomic medium, their projections on the longitudinal z axis are described as

$$\begin{aligned} E_p^{(+)}(z,t) &= E_p(z)e^{i(-k_p z\cos\theta-\omega_p t)}, \\ E_c^{(+)}(z,t) &= E_c(z)e^{i(k_c z\cos\theta-\omega_c t)}, \end{aligned} \tag{1}$$

where k_p (k_c) is the wave number of the pump (coupling) laser field. We treat the single-transverse-mode Stokes and anti-Stokes fields as quantized operators:

$$\begin{aligned} \hat{E}_s^{(+)}(z,t) &= \sqrt{\frac{2\hbar\omega_{s0}}{c\varepsilon_0 A}}\hat{a}_s(z,t) \\ &= \frac{1}{\sqrt{2\pi}}\sqrt{\frac{2\hbar\omega_{s0}}{c\varepsilon_0 A}}\int d\omega_s \hat{a}_s(\omega_s)e^{i[-\int_0^z k_s(z')dz'-\omega_s t]}, \\ \hat{E}_{\rm as}^{(+)}(z,t) &= \sqrt{\frac{2\hbar\omega_{\rm as0}}{c\varepsilon_0 A}}\hat{a}_{\rm as}(z,t) \\ &= \frac{1}{\sqrt{2\pi}}\sqrt{\frac{2\hbar\omega_{\rm as0}}{c\varepsilon_0 A}}\int d\omega_{\rm as} \hat{a}_{\rm as}(\omega_{\rm as})e^{i[\int_0^z k_{\rm as}(z')dz'-\omega_{\rm as} t]}. \end{aligned} \tag{2}$$

Here c is the speed of light in vacuum, ε_0 is the vacuum permittivity, A is the single-mode cross-sectional area, and $\omega_{\rm as0}$ (ω_{s0}) is the central frequency of the anti-Stokes (Stokes) photon. $k_s(z')$ and $k_{\rm as}(z')$ are the wave vectors of the Stokes and anti-Stokes fields inside the atomic medium, respectively. $\hat{a}_s(\omega_s)$ [$\hat{a}_{\rm as}(\omega_{\rm as})$] annihilates a Stokes (anti-Stokes) photon of frequency ω_s ($\omega_{\rm as}$), and it satisfies the commutation relation

$$[\hat{a}_s(\omega),\hat{a}_s^\dagger(\omega')] = [\hat{a}_{\rm as}(\omega),\hat{a}_{\rm as}^\dagger(\omega')] = \delta(\omega-\omega'). \tag{3}$$

The interaction Hamiltonian that describes the SFWM process is

$$\begin{aligned} \hat{H}_I = \frac{\varepsilon_0 A}{4}\int_{-\frac{L}{2}}^{\frac{L}{2}} dz\, \chi^{(3)}(z)[E_p^{(+)}(z,t)E_c^{(+)}(z,t) \\ \times \hat{E}_{\rm as}^{(-)}(z,t)\hat{E}_s^{(-)}(z,t)] + \text{H.c.}, \end{aligned} \tag{4}$$

where $\chi^{(3)}(z)$ is the third-order nonlinear susceptibility and is given in Eq. (59) in Sec. III. $E_s^{(-)}(z,t)$ and $E_{\rm as}^{(-)}(z,t)$ are the Hermitian conjugates of the Stokes and anti-Stokes fields [Eq. (2)], respectively. Substituting the electric fields in Eqs. (1) and (2) into Eq. (4) gives

$$\begin{aligned} \hat{H}_I = \frac{\hbar\sqrt{\omega_{s0}\omega_{\rm as0}}}{4\pi c}\int d\omega_s d w_{\rm as}\int_{-\frac{L}{2}}^{\frac{L}{2}} dz\, \chi^{(3)}(z)E_p(z)E_c(z) \\ \times e^{-i\int_0^z \Delta k(z')dz'}\hat{a}_{\rm as}^\dagger(\omega_{\rm as})\hat{a}_s^\dagger(\omega_s)e^{-i(\omega_p+\omega_c-\omega_s-\omega_{\rm as})t} + \text{H.c.}, \end{aligned} \tag{5}$$

where

$$\Delta k(z') \equiv k_{\rm as}(z') - k_s(z') - (k_c - k_p)\cos\theta \tag{6}$$

is the phase-mismatching term in the atomic cloud. When $\Delta k(z') = 0$, $\vec{k}_{\rm as} + \vec{k}_s = \vec{k}_c + \vec{k}_p$, the phase-match condition holds perfectly.

The two-photon state $|\Psi\rangle$ can be computed in the first-order perturbation theory as

$$|\Psi\rangle = -\frac{i}{\hbar}\int_{-\infty}^{\infty} \hat{H}_I|0\rangle\, dt. \tag{7}$$

Substituting Eq. (5) into Eq. (7) and integrating over t gives

$$|\Psi\rangle = \frac{\sqrt{\omega_{s0}\omega_{\rm as0}}}{2ic}\int d\omega_{\rm as}\int_{-\frac{L}{2}}^{\frac{L}{2}} dz[\chi^{(3)}(z)E_p(z)E_c(z) \times e^{-i\int_0^z \Delta k(z')dz'}\hat{a}_{\rm as}^\dagger(\omega_{\rm as})\hat{a}_s^\dagger(\omega_p+\omega_c-\omega_{\rm as})|0\rangle]. \tag{8}$$

Note that from Eq. (7) to Eq. (8), we have made use of the time integral, $\int_{-\infty}^{\infty} e^{-i(\omega_p+\omega_c-\omega_s-\omega_{\rm as})t}dt = 2\pi\delta(\omega_p+\omega_c-\omega_s-\omega_{\rm as})$, which expresses energy conservation of the four-wave mixing process and leads to the frequency entanglement of the two-photon state.

In our setup in Fig. 1, we neglect the free space propagation (which only causes time shift in measurements) and place the Stokes photon detector D_s at $z = -L/2$ and the anti-Stokes photon detector $D_{\rm as}$ at $z = L/2$. The annihilation operators at these two boundaries are

$$\begin{aligned}\hat{a}_s(t) &= \frac{1}{\sqrt{2\pi}}\int d\omega\hat{a}_s(\omega)e^{i\int_0^{\frac{L}{2}} k_s(-z')dz'-i\omega t},\\ \hat{a}_{\rm as}(t) &= \frac{1}{\sqrt{2\pi}}\int d\omega\hat{a}_{\rm as}(\omega)e^{i\int_0^{\frac{L}{2}} k_{\rm as}(z')dz'-i\omega t}.\end{aligned} \tag{9}$$

The two-photon Glauber correlation function can be computed from

$$\begin{aligned}G^{(2)}(t_s,t_{\rm as}) &= \langle\Psi|\hat{a}_{\rm as}^\dagger(t_{\rm as})\hat{a}_s^\dagger(t_s)\hat{a}_s(t_s)\hat{a}_{\rm as}(t_{\rm as})|\Psi\rangle\\ &= |\langle 0|\hat{a}_s(t_s)\hat{a}_{\rm as}(t_{\rm as})|\Psi\rangle|^2\\ &\equiv |\Psi(t_s,t_{\rm as})|^2,\end{aligned} \tag{10}$$

where $\Psi(t_s,t_{\rm as})$ is the Stokes–anti-Stokes biphoton amplitude. Substituting Eqs. (8) and (9) into Eq. (10), the biphoton amplitude becomes

$$\Psi(t_s,t_{\rm as}) = \frac{\sqrt{\omega_{s0}\omega_{\rm as0}}}{i4\pi c}\int d\omega_{\rm as}d\omega_s'd\omega_{\rm as}'\int_{-\frac{L}{2}}^{\frac{L}{2}} dz\{\chi^{(3)}(z)E_p(z)E_c(z)e^{-i\int_0^z\Delta k(z')dz'}e^{i\int_0^{\frac{L}{2}}[k_s(-z')+k_{\rm as}(z')]dz'}e^{-i\omega_s't_s-i\omega_{\rm as}'t_{\rm as}} \times\langle 0|\hat{a}_s(\omega_s')\hat{a}_{\rm as}(\omega_{\rm as}')\hat{a}_{\rm as}^\dagger(\omega_{\rm as})\hat{a}_s^\dagger(\omega_p+\omega_c-\omega_{\rm as})|0\rangle\}. \tag{11}$$

Using the commutation relation of Eq. (3), we have $\langle 0|\hat{a}_s(\omega_s')\hat{a}_{\rm as}(\omega_{\rm as}')\hat{a}_{\rm as}^\dagger(\omega_{\rm as})\hat{a}_s^\dagger(\omega_p+\omega_c-\omega_{\rm as})|0\rangle = \delta(\omega_s'-\omega_p-\omega_c+\omega_{\rm as})\delta(\omega_{\rm as}'-\omega_{\rm as})$. Integrating over $d\omega_s'$ and $d\omega_{\rm as}'$, the biphoton amplitude is now

$$\Psi(t_s,t_{\rm as}) = \frac{\sqrt{\omega_{s0}\omega_{\rm as0}}}{i4\pi c}\int d\omega_{\rm as}\int_{-\frac{L}{2}}^{\frac{L}{2}} dz\{\chi^{(3)}(z)E_p(z)E_c(z)e^{-i\int_0^z\Delta k(z')dz'}e^{i\int_0^{\frac{L}{2}}[k_s(-z')+k_{\rm as}(z')]dz'}e^{-i(\omega_p+\omega_c)t_s-i\omega_{\rm as}\tau}\}, \tag{12}$$

where $\tau \equiv t_{\rm as} - t_s$.

The wave numbers of the Stokes and anti-Stokes photons can be described as

$$\begin{aligned}k_s(z) &= \frac{\omega_{s0}}{c}\sqrt{1+\chi_s(z,\omega_{s0}-\varpi)},\\ k_{\rm as}(z) &= \frac{\omega_{\rm as0}}{c}\sqrt{1+\chi_{\rm as}(z,\omega_{\rm as0}+\varpi)},\end{aligned} \tag{13}$$

where ω_{s0} ($\omega_{\rm as0}$) is the Stokes (anti-Stokes) photon central frequency, and $-\varpi$ (ϖ) is the Stokes (anti-Stokes) frequency detuning. $\chi_s(z,\omega_{s0}-\varpi)$ and $\chi_{\rm as}(z,\omega_{\rm as0}+\varpi)$, given in Sec. III [Eqs. (56) and (57)], are the linear susceptibilities of the Stokes and anti-Stokes fields, respectively. Note that k_s and $k_{\rm as}$ are also functions of ϖ through $\chi_s(z,\omega_{s0}-\varpi)$ and $\chi_{\rm as}(z,\omega_{\rm as0}+\varpi)$. Making use of $\omega_p+\omega_c = \omega_{s0}+\omega_{\rm as0}$, we can rewrite Eq. (12) as

$$\Psi(t_s,t_{\rm as}) = \psi(\tau)e^{-i(\omega_{\rm as0}t_{\rm as}+\omega_{s0}t_s)}, \tag{14}$$

where the biphoton relative wave amplitude is given by

$$\psi(\tau) \equiv \frac{\sqrt{\omega_{s0}\omega_{\rm as0}}}{i4\pi c}\int d\varpi\, F(\varpi)Q(\varpi)e^{-i\varpi\tau}. \tag{15}$$

Here

$$F(\varpi) \equiv \int_{-\frac{L}{2}}^{\frac{L}{2}} dz\chi^{(3)}(z)E_p(z)E_c(z)e^{-i\int_0^z\Delta k(z')dz'}, \tag{16}$$

$$Q(\varpi) = e^{i\int_0^{\frac{L}{2}}[k_s(-z')+k_{\rm as}(z')]dz'}. \tag{17}$$

1. No z dependence

If the atomic cloud is homogeneous, the pump and coupling lasers have uniform electric fields in the atomic cloud, Eq. (16) can be computed analytically, and the result is

$$F(\varpi) = L\chi^{(3)}(\varpi)E_pE_c{\rm sinc}\left(\frac{\Delta kL}{2}\right), \tag{18}$$

where $\Delta k = k_{\rm as} - k_s - (k_c-k_p)\cos\theta$ is a function of ϖ only. The biphoton relative wave function $\psi(\tau)$ is now

$$\psi(\tau) = \frac{\sqrt{\omega_{s0}\omega_{\rm as0}}}{i4\pi c}LE_pE_c\int d\varpi\ \chi^{(3)}(\varpi)\,{\rm sinc}\left(\frac{\Delta kL}{2}\right) \times e^{i(k_s+k_{\rm as})L/2}e^{-i\varpi\tau}. \tag{19}$$

Here k_s and $k_{\rm as}$ are given by Eq. (13). As the first-order susceptibilities χ_s and $\chi_{\rm as}$ have no z dependence, k_s and $k_{\rm as}$

are functions of ϖ only, independent of z. The expression of the biphoton amplitude agrees with the previous work by Du *et al.* [25].

For a weak pump laser that is far detuned, $\chi_s \approx 0$ and Δk depends on the group velocity of anti-Stokes photons V_g as $\Delta k \approx \varpi / V_g$. In this case, Eq. (19) is proportional to the rectangular function $\Pi(\tau; 0, L/V_g)$, which ranges from $\tau = 0$ to L/V_g [25]. Physically, this rectangular waveform can be explained as follows [25,32]: the Stokes and anti-Stokes photons are always produced in pairs by the same atom in the atomic cloud. In our experimental setup as illustrated in Fig. 1, when the photon pairs are produced at the surface $z = L/2$, an anti-Stokes photon does not need to go through the atomic medium to arrive at the anti-Stokes detector $D_{\rm as}$. For a Stokes photon, $\chi_s \approx 0$ and k_s is approximately the wave vector in vacuum. Therefore, the Stokes photon travels in the atomic medium at nearly the same velocity as in vacuum. As the length of the atomic medium is very short, the travel time to reach detector D_s is negligible. As such, both Stokes and anti-Stokes detectors register a photon almost simultaneously. When the photon pairs are produced at the other surface, $z = -L/2$, an anti-Stokes photon has to go through the medium at group velocity V_g to reach detector $D_{\rm as}$, while a Stokes photon does not have to travel through the medium in order to reach detector D_s. After D_s registers the Stokes photon, a delay $\tau_g = L/V_g$ later, the anti-Stokes photon reaches detector $D_{\rm as}$. When photon pairs are produced between $-L/2$ and $L/2$, the delay time is between 0 and τ_g. As every atom in the cloud has the same third-order susceptibility and experiences the same pump and coupling laser fields, the probability of producing the photon pairs at every point in the atomic medium is the same. This results in a rectangular waveform.

2. *The atomic density is not uniform*

Let us consider the case where the atoms are not distributed uniformly along the longitudinal direction. Here we limit the discussion to cases where the atomic density varies with the constraint that the OD is fixed. Once an experimental setup is complete, the OD is a fixed number and the atomic density can be inferred through the OD. We are also particularly interested in the low-parametric-gain regime where the pump laser is weak and far detuned as illustrated in Fig. 1.

The atomic density is described as $N(z) = N_0 f_N(z)$, where N_0 is the mean atomic density and $f_N(z)$ is the atomic density profile function ($\int_{-L/2}^{L/2} f_N(z)dz = L$). The optical depth is given as $\mathrm{OD} = \int_{-L/2}^{L/2} N(z)\sigma_{13}dz = N_0\sigma_{13}L$, where σ_{13} is the on-resonance absorption cross section at the anti-Stokes transition. The profile function $f_N(z)$ appears in both the linear and the third-order nonlinear susceptibilities [Eqs. (56)–(59)]. Write $\chi_{\rm as}(z) = \bar{\chi}_{\rm as} f_N(z)$ and $\chi^{(3)}(z) = \bar{\chi}^{(3)} f_N(z)$, with $\bar{\chi}_{\rm as}$ and $\bar{\chi}^{(3)}$ being the parts that are independent of z; from Eq. (16) we have

$$F(\varpi) = \bar{\chi}^{(3)} E_p E_c \int_{-\frac{L}{2}}^{\frac{L}{2}} dz f_N(z) e^{-i\int_0^z \Delta k(z')dz'}. \tag{20}$$

When the pump laser is weak and far detuned, the Stokes field is weak and $\chi_s \approx 0$, the phase-matching term $\Delta k(z') \approx \bar{\Delta k} f_N(z')$, with $\bar{\Delta k}$ defined as $\bar{\Delta k} \equiv \omega_{\rm as0}/(2c)\,\bar{\chi}_{\rm as}$, which does not vary with z. Equation (20) becomes

$$F(\varpi) = \bar{\chi}^{(3)} E_p E_c \int_{-\frac{L}{2}}^{\frac{L}{2}} dz G'(z) e^{-i\bar{\Delta k} G(z)}, \tag{21}$$

where

$$G(z) \equiv \int_0^z f_N(z')dz' \tag{22}$$

and $G'(z)$ is its derivative. After performing the integration on z in Eq. (21), taking into account that the OD is fixed (or $\int_{-L/2}^{L/2} f_N(z)dz = L$), and ignoring the vacuum phase-mismatching term [$(\Delta k)_{\rm vacuum} \approx 0$], we have

$$\begin{aligned} F(\varpi) =& \bar{\chi}^{(3)} E_p E_c L\ \mathrm{sinc}\left(\frac{\bar{\Delta k} L}{2}\right) e^{i\bar{\Delta k}(L/2-\beta)}, \\ Q(\varpi) =& e^{i(k_{s0}+k_{\rm as0})L/2} e^{i\bar{\Delta k}\beta}, \end{aligned} \tag{23}$$

where $\beta \equiv \int_0^{L/2} f_N(z')dz'$. Note that by substituting Eq. (23) into Eq. (15), we recover Eq. (19), which describes the case when the atomic density is uniform.

Let us try to understand intuitively why the biphoton waveform is independent of the atomic distribution. The biphoton waveform depends on two factors: (i) the probability of biphoton generation by atoms in the atomic cloud and (ii) the time required for the photons to propagate through the atomic cloud to the detector. When the atomic distribution changes from uniform to nonuniform with a distribution, the probability of emitting photon pairs should follow this distribution. That is, in space where there are more atoms, the probability of emitting photons pairs increases. At the same time, the group velocity in this densely populated space decreases and thus photons need more time to travel through this space to reach the detector. As the coincidence counting rate is in fact the probability of generating photon pairs divided by the time for the photons to reach the detector, the effect of longer travel time washes out that of the higher probability density. As a result, the biphoton waveform is not sensitive to the atomic density distribution profile.

Note that the above discussion is valid only when (i) the atomic density varies in the longitudinal direction with the constraint that the OD is fixed, and (ii) the pump laser is weak and far detuned. Both conditions are of interest for our ongoing experiments. If (i) is not satisfied but (ii) is, our numerical analysis shows that the waveform will still be rectangle-like as in the case of a uniform atomic density. But the group delay time is changed, as it is determined by $\tau_g = (2\gamma_{13}/|\Omega_c^2|)\mathrm{OD}$ [25].

3. *The pump laser has a z profile*

If the pump laser has a nonuniform z profile, namely, $E_p(z) = E_p f_p(z)$, the coupling laser has a uniform profile, and the atomic cloud is homogeneous, Eq. (16) becomes

$$F(\varpi) = E_p E_c \chi^{(3)}(\varpi) \int_{-\frac{L}{2}}^{\frac{L}{2}} dz f_p(z) e^{-i\int_0^z \Delta k(z')dz'}. \tag{24}$$

Here $\chi^{(3)}(\varpi)$ does not depend on the pump profile [see Eq. (59)]. When the pump laser is weak and far detuned, the

linear susceptibility of the Stokes field $\chi_s \approx 0$, and

$$\Delta k(z') \approx \frac{\varpi}{V_g}, \tag{25}$$

where V_g is the group velocity of the anti-Stokes photons. Now Eq. (17) can be approximated as

$$Q(\varpi) \approx e^{i(k_{s0}+k_{\mathrm{as}0})\frac{L}{2}} e^{i\varpi L/(2V_g)}, \tag{26}$$

where $k_{s0} = \omega_{s0}/c$ is the central wave number of the Stokes photons and $k_{\mathrm{as}0} = \omega_{\mathrm{as}0}/c$ is the central wave number of the anti-Stokes photons. Equation (24), at the same time, can be approximated by

$$F(\varpi) \approx \chi^{(3)} E_p E_c \int_{-\frac{L}{2}}^{\frac{L}{2}} dz f_p(z) e^{-i\varpi z/V_g}. \tag{27}$$

Substituting Eqs. (26) and (27) into Eq. (12) results in

$$\psi(\tau) \approx \frac{\sqrt{\omega_{s0}\omega_{\mathrm{as}0}}}{i4\pi c} E_p E_c e^{i(k_{s0}+k_{\mathrm{as}0})\frac{L}{2}} \times \int_{-\frac{L}{2}}^{\frac{L}{2}} dz f_p(z) \widetilde{\chi^{(3)}}\left(\tau + \frac{z}{V_g} - \frac{L}{2V_g}\right). \tag{28}$$

Here

$$\widetilde{\chi^{(3)}}\left(\tau + \frac{z}{V_g} - \frac{L}{2V_g}\right) \equiv \int d\varpi\ \chi^{(3)}(\varpi) e^{-i\varpi(\tau+\frac{z}{V_g}-\frac{L}{2V_g})}. \tag{29}$$

With the change of integration variable from z to t as $t = \tau + z/V_g - L/(2V_g)$, integration in the space domain in Eq. (28) changes to integration in the time domain:

$$\psi(\tau) = \frac{\sqrt{\omega_{s0}\omega_{\mathrm{as}0}}}{i4\pi c} E_p E_c V_g e^{i(k_{s0}+k_{\mathrm{as}0})\frac{L}{2}} \times \int_{\tau-\frac{L}{V_g}}^{\tau} dt f_p\left(\frac{L}{2} + V_g(t-\tau)\right) \widetilde{\chi^{(3)}}(t). \tag{30}$$

This is a convolution of the pump laser profile in the space domain $f_p(z)$ and the third-order susceptibility in the time domain. In the group delay regime where the EIT window is much narrower than the $\chi^{(3)}$ spectrum, we can approximate $\chi^{(3)}(\varpi) \simeq \chi^{(3)}(0)$ in the integral, (29). Then Eq. (30) reduces to

$$\psi(\tau) = \frac{\sqrt{\omega_{s0}\omega_{\mathrm{as}0}}}{i2c} E_p E_c \chi^{(3)}(0) V_g e^{i(k_{s0}+k_{\mathrm{as}0})\frac{L}{2}} f_p\left(\frac{L}{2} - V_g\tau\right). \tag{31}$$

The argument in function $f_p(\frac{L}{2} - V_g\tau)$ suggests that the space-domain function $f_p(z)$ is mapped to the time-domain function $\psi(\tau)$ scaled with the anti-Stokes group delay. Note that if the space-domain function $f_p(z)$ is a rectangular function, that is, when the pump power is uniform, we will have a time-domain rectangular $\psi(\tau)$.

The assumption that Δk can be approximated by Eq. (25) is valid when the loss in the medium is negligible. To account for the loss, we have to include an imaginary part α to the anti-Stokes wave number as $k_{\mathrm{as}} \approx k_{\mathrm{as}0} + \varpi/V_g + i\alpha$. This imaginary part will then appear in $Q(\varpi)$ as an exponential decay factor, $\exp(-\alpha L/2)$.

4. The coupling laser has a z profile

If the coupling laser has a nonuniform profile in the z direction, the Rabi frequency, $\Omega_c(z) \propto E_c(z)$, depends on z. As a result, the linear and third-order responses of the atomic cloud depend on z [see Eqs. (56)–(59)], as well as the wave vectors. The analytical solution is too complicated. We discuss the numerical results in Sec. III.

B. Heisenberg picture

Now we turn to the Heisenberg picture where the vacuum-state vector is time invariant and the system is described by the evolution of the Stokes and anti-Stokes field operators. The coupling of the Stokes and anti-Stokes fields to the environment is included through Langevin force operators. In this picture, the space- and time-dependent Stokes and anti-Stokes field operators can be expressed as

$$\begin{aligned} E_s^{(+)}(z,t) &= \sqrt{\frac{2\hbar\omega_{s0}}{c\varepsilon_0 A}} \hat{a}_s(z,t) e^{i(-k_{s0}z-\omega_{s0}t)}, \\ E_{\mathrm{as}}^{(+)}(z,t) &= \sqrt{\frac{2\hbar\omega_{\mathrm{as}0}}{c\varepsilon_0 A}} \hat{a}_{\mathrm{as}}(z,t) e^{i(k_{\mathrm{as}0}z-\omega_{\mathrm{as}0}t)}. \end{aligned} \tag{32}$$

The slowly varying envelope field operators $\hat{a}_s(z,t)$ and $\hat{a}_{\mathrm{as}}(z,t)$ in the time domain are related to the frequency-domain operators $\hat{a}_s(z,-\varpi)$ and $\hat{a}_{\mathrm{as}}(z,\varpi)$ through a Fourier transform,

$$\begin{aligned} \hat{a}_s(z,t) &= \frac{1}{\sqrt{2\pi}} \int d\varpi\ \hat{a}_s(z,\varpi) e^{-i\varpi t}, \\ \hat{a}_{\mathrm{as}}(z,t) &= \frac{1}{\sqrt{2\pi}} \int d\varpi\ \hat{a}_{\mathrm{as}}(z,\varpi) e^{-i\varpi t}, \end{aligned} \tag{33}$$

which is governed by the coupled Heisenberg-Langevin equations under the slowly varying envelope approximation,

$$\begin{aligned} &\frac{\partial \hat{a}_{\mathrm{as}}(z,\varpi)}{\partial z} + \left(\alpha_{\mathrm{as}} - i\frac{\Delta k_0}{2}\right)\hat{a}_{\mathrm{as}}(z,\varpi) - \kappa_{\mathrm{as}}\hat{a}_s^\dagger(z,-\varpi) = \hat{F}_{\mathrm{as}}, \\ &\frac{\partial \hat{a}_s^\dagger(z,-\varpi)}{\partial z} + \left(g_s + i\frac{\Delta k_0}{2}\right)\hat{a}_s^\dagger(z,-\varpi) - \kappa_s\hat{a}_{\mathrm{as}}(z,\varpi) = \hat{F}_s^\dagger. \end{aligned} \tag{34}$$

Here

$$\begin{aligned} \alpha_{\mathrm{as}}(z,\varpi) &= -\frac{i\omega_{\mathrm{as}}}{2c}\chi_{\mathrm{as}}(z,\omega_{\mathrm{as}0}+\varpi), \\ g_s(z,\varpi) &= -\frac{i\omega_s}{2c}\chi_s^*(z,\omega_{s0}-\varpi), \\ \kappa_{\mathrm{as}}(z,\varpi) &= \frac{i\omega_{\mathrm{as}}}{2c}\chi_{\mathrm{as}}^{(3)}(z,\omega_{\mathrm{as}0}+\varpi)E_p(z)E_c(z), \\ \kappa_s(z,\varpi) &= \frac{i\omega_s}{2c}\chi_s^{(3)*}(z,\omega_{s0}-\varpi)E_p^*(z)E_c^*(z), \end{aligned} \tag{35}$$

and F_{as} and $F_s^\dagger$ are the contributions from the Langevin noises. They are given by

$$\begin{aligned} \hat{F}_{\mathrm{as}} &= \beta_{21}^{\mathrm{as}}\hat{f}_{\sigma_{21}^\dagger} + \beta_{24}^{\mathrm{as}}\hat{f}_{\sigma_{24}^\dagger} + \beta_{31}^{\mathrm{as}}\hat{f}_{\sigma_{31}^\dagger} + \beta_{34}^{\mathrm{as}}\hat{f}_{\sigma_{34}^\dagger}, \\ \hat{F}_s^\dagger &= \beta_{21}^{s}\hat{f}_{\sigma_{21}^\dagger} + \beta_{24}^{s}\hat{f}_{\sigma_{24}^\dagger} + \beta_{31}^{s}\hat{f}_{\sigma_{31}^\dagger} + \beta_{34}^{s}\hat{f}_{\sigma_{34}^\dagger}. \end{aligned} \tag{36}$$

Here $\hat{f}_{\alpha_i^\dagger}$ are Langevin force operators, and $\beta_{\alpha_i}^{\rm as}$ and $\beta_{\alpha_i}^{s}$ ($\alpha_i = 21,24,31,34$) are the noise coefficients. Detailed expressions for the noise coefficients are given in the Appendix.

$\Delta k_0 \equiv k_{\rm as0} - k_{s0} - (k_c - k_p)\cos\theta$ is the phase-mismatching term in vacuum. The expressions for susceptibilities $\chi_{\rm as}(z,\omega_{\rm as0}+\varpi)$, $\chi_s(z,\omega_{s0}-\varpi)$, $\chi_{\rm as}^{(3)}(z,\omega_{\rm as0}+\varpi)$, and $\chi_s^{(3)}(z,\omega_{s0}-\varpi)$ are given in Sec. III [Eqs. (56) to (59)]. Defining $l \equiv L/2$, we have the following boundary conditions (vacuum at $z=\pm l$) for the coupled differential equations (34):

$$[\hat{a}_s(l,\varpi),\hat{a}_s^\dagger(l,\varpi')] = [\hat{a}_{\rm as}(-l,\varpi),\hat{a}_{\rm as}^\dagger(-l,\varpi')] = \delta(\varpi-\varpi'), \tag{37}$$

$$\langle \hat{a}_s^\dagger(l,\varpi)\hat{a}_s(l,\varpi)\rangle = \langle \hat{a}_{\rm as}^\dagger(-l,\varpi)\hat{a}_{\rm as}(-l,\varpi)\rangle = 0. \tag{38}$$

As shown in the Appendix, the general solution to Eqs. (34) at the output surface can be written as

$$\begin{pmatrix} \hat{a}_{\rm as}(l,\varpi) \\ \hat{a}_s^\dagger(-l,-\varpi)\end{pmatrix} = \begin{pmatrix} A(\varpi) & B(\varpi) \\ C(\varpi) & D(\varpi)\end{pmatrix}\begin{pmatrix} \hat{a}_{\rm as}(-l,\varpi) \\ \hat{a}_s^\dagger(l,-\varpi)\end{pmatrix} + \sum_{\alpha_i}\int_{-l}^{l} dz \begin{pmatrix} P_{\alpha_i} \\ Q_{\alpha_i}\end{pmatrix}\hat{f}_{\alpha_i^\dagger}. \tag{39}$$

P_{α_i} and Q_{α_i} ($\alpha_i = 21, 24, 31, 34$) are functions of z and ϖ and contain contributions from Langevin noises (see the Appendix for their expressions).

The Glauber correlation function can be calculated from

$$G_{s,\rm as}^{(2)}(\tau) \equiv \langle \hat{a}_{\rm as}^\dagger(l,t_s+\tau)\hat{a}_s^\dagger(-l,t_s)\hat{a}_s(-l,t_s)\hat{a}_{\rm as}(l,t_s+\tau)\rangle = |\psi(\tau)|^2 + R_{\rm as}R_s. \tag{40}$$

Here the Stokes and anti-Stokes two-photon relative wave amplitude on the output surface ($z=\pm l$) is

$$\psi(\tau \equiv t_{\rm as}-t_s) \equiv \langle \hat{a}_s(-l,t_s)\hat{a}_{\rm as}(l,t_{\rm as})\rangle = \int \frac{d\varpi}{2\pi} e^{-i\varpi\tau}\left[B(\varpi)D^*(\varpi) + \sum_{\alpha_i,\alpha_j}\int_{-l}^{l} dz\, Q_{\alpha_i}^* D_{\alpha_i,\alpha_j^\dagger} P_{\alpha_j}\right], \tag{41}$$

where $D_{\alpha_i,\alpha_j^\dagger}$ are diffusion coefficients (see the Appendix for details). The generation rates of the Stokes photons and anti-Stokes photons are given by

$$R_s \equiv \langle \hat{a}_s^\dagger(-l,t_s)\hat{a}_s(-l,t_s)\rangle = \int \frac{d\varpi}{2\pi}\left(|C(\varpi)|^2 + \sum_{\alpha_i,\alpha_j}\int_{-l}^{l} dz\, Q_{\alpha_i} D_{\alpha_i^\dagger,\alpha_j} Q_{\alpha_j}^*\right), \tag{42}$$

$$R_{\rm as} \equiv \langle \hat{a}_{\rm as}^\dagger(l,t_{\rm as})\hat{a}_{\rm as}(l,t_{\rm as})\rangle = \int \frac{d\varpi}{2\pi}\left(|B(\varpi)|^2 + \sum_{\alpha_i,\alpha_j}\int_{-l}^{l} dz\, P_{\alpha_i}^* D_{\alpha_i,\alpha_j^\dagger} P_{\alpha_j}\right),$$

respectively. The $R_{\rm as}R_s$ term in Eq. (40) results from accidental coincidence between uncorrelated photons because the photon pairs are produced stochastically and the time separation between different pairs is unpredictable. The detailed derivation is given in the Appendix.

The photon pair generation rate can be computed as

$$R = \int |\psi(\tau)|^2 d\tau = \int \frac{d\varpi}{2\pi}\left|B(\varpi)D^*(\varpi) + \sum_{\alpha_i,\alpha_j}\int_{-l}^{l} dz\, Q_{\alpha_i}^* D_{\alpha_i,\alpha_j^\dagger} P_{\alpha_j}\right|^2. \tag{43}$$

This is the area under the Stokes–anti-Stokes correlation function minus the uncorrelated background.

Note that we can also define anti-Stokes and Stokes biphoton amplitude as

$$\psi(\tau) \equiv \langle \hat{a}_{\rm as}(l,t_{\rm as})\hat{a}_s(-l,t_s)\rangle = \int \frac{d\varpi}{2\pi} e^{-i\varpi\tau}\left[A(\varpi)C^*(\varpi) + \sum_{\alpha_i,\alpha_j}\int_{-l}^{l} dz\, P_{\alpha_i} D_{\alpha_i^\dagger,\alpha_j} Q_{\alpha_j}^*\right]. \tag{44}$$

With the contribution from Langevin noise, Eqs (41) and (44) should give the same results numerically. This has been verified by our numerical calculations for a wide range of parameters. Note that when the pump is weak and far detuned, the majority of the atomic population is in the ground state. The diffusion coefficients $D_{\alpha_i,\alpha_j^\dagger}$, which appear in Eq. (41), are very small, as they only depend on the excited-state population (see the Appendix for details). This makes the contribution to Eq. (41) from Langevin noise negligible. However, the diffusion coefficients $D_{\alpha_i^\dagger,\alpha_j}$, which appear in Eq. (44), are large, as they also depend on the ground-state population. As a result, the contribution from Langevin noise to Eq. (44) is large. Therefore in the following discussion, for convenience, we take the following approximation to analyze the bphoton temporal wave function:

$$\psi(\tau) \simeq \int \frac{d\varpi}{2\pi} B(\varpi)D^*(\varpi)e^{-i\varpi\tau}. \tag{45}$$

The normalized cross-correlation function of Stokes–anti-Stokes photons is

$$g_{s,\rm as}^{(2)}(\tau) \equiv \frac{\langle \hat{a}_{\rm as}^\dagger(l,t_s+\tau)\hat{a}_s^\dagger(-l,t_s)\hat{a}_s(-l,t_s)\hat{a}_{\rm as}(l,t_s+\tau)\rangle}{\langle \hat{a}_{\rm as}^\dagger(l,t_s+\tau)\hat{a}_{\rm as}(l,t_s+\tau)\rangle\langle \hat{a}_s^\dagger(-l,t_s)\hat{a}_s(-l,t_s)\rangle} = \frac{G_{s,\rm as}^{(2)}(\tau)}{R_{\rm as}R_s} = 1 + \frac{|\psi(\tau)|^2}{R_{\rm as}R_s}. \tag{46}$$

The normalized autocorrelation function of the anti-Stokes photons is

$$g^{(2)}_{\mathrm{as,as}}(\tau)=\frac{\langle\hat{a}^{\dagger}_{\mathrm{as}}(l,0)\hat{a}^{\dagger}_{\mathrm{as}}(l,\tau)\hat{a}_{\mathrm{as}}(l,\tau)\hat{a}_{\mathrm{as}}(l,0)\rangle}{\langle\hat{a}^{\dagger}_{\mathrm{as}}(l,0)\hat{a}_{\mathrm{as}}(l,0)\rangle\langle\hat{a}^{\dagger}_{\mathrm{as}}(l,\tau)\hat{a}_{\mathrm{as}}(l,\tau)\rangle}=\frac{\left|\int\frac{d\varpi}{2\pi}e^{-i\varpi\tau}\left(|B(\varpi)|^2+\sum_{\alpha_i,\alpha_j}\int_{-l}^{l}dz\,P^{*}_{\alpha_i}D_{\alpha_i,\alpha_j^{\dagger}}P_{\alpha_j}\right)\right|^2}{\left[\int\frac{d\varpi}{2\pi}\left(|B(\varpi)|^2+\sum_{\alpha_i,\alpha_j}\int_{-l}^{l}dz\,P^{*}_{\alpha_i}D_{\alpha_i,\alpha_j^{\dagger}}P_{\alpha_j}\right)\right]^2}+1, \tag{47}$$

and that of the Stokes photons is

$$g^{(2)}_{s,s}(\tau)=\frac{\langle\hat{a}^{\dagger}_{s}(l,0)\hat{a}^{\dagger}_{s}(l,\tau)\hat{a}_{s}(l,\tau)\hat{a}_{s}(l,0)\rangle}{\langle\hat{a}^{\dagger}_{s}(l,0)\hat{a}_{s}(l,0)\rangle\langle\hat{a}^{\dagger}_{s}(l,\tau)\hat{a}_{s}(l,\tau)\rangle}=\frac{\left|\int\frac{d\varpi}{2\pi}e^{-i\varpi\tau}\left(|C(\varpi)|^2+\sum_{\alpha_i,\alpha_j}\int_{-l}^{l}dz\,Q_{\alpha_i}D_{\alpha_i^{\dagger},\alpha_j}Q^{*}_{\alpha_j}\right)\right|^2}{\left[\int\frac{d\varpi}{2\pi}\left(|C(\varpi)|^2+\sum_{\alpha_i,\alpha_j}\int_{-l}^{l}dz\,Q_{\alpha_i}D_{\alpha_i^{\dagger},\alpha_j}Q^{*}_{\alpha_j}\right)\right]^2}+1. \tag{48}$$

It is clear that Eqs. (47) and (48) are the autocorrelation functions for multimode chaotic light sources with $g^{(2)}_{\mathrm{as,as}}(0)=g^{(2)}_{s,s}(0)=2$. For classical light, there is the Cauchy-Schwarz inequality $[g^{(2)}_{s,\mathrm{as}}(\tau)]^2/[g^{(2)}_{s,s}(0)g^{(2)}_{\mathrm{as,as}}(0)]\leqslant 1$ [33]. Therefore violation of the Cauchy-Schwarz inequality is a measure of the nonclassical property of the biphoton source, which requires $[g^{(2)}_{s,\mathrm{as}}(\tau)]_{\max}>2$.

No z dependence

When the atomic cloud is homogeneous, the pump and coupling laser beams have uniform intensities in the atomic cloud; i.e., when $N(z)=N_0$, $E_p(z)=E_p$, and $E_c(z)=E_c$, there will be no z dependence for α_{as}, g_s, κ_{as}, or κ_s as well in Eq. (34). In this case the coupled equation, (34), can be solved analytically. The result is

$$B(\varpi)=\frac{2\kappa_{\mathrm{as}}}{q+Q\coth(lQ)}, \tag{49}$$

$$D(\varpi)=\frac{Q\exp[(g_s+\alpha_{\mathrm{as}})l]}{q\sinh(lQ)+Q\cosh(lQ)}. \tag{50}$$

Here $q\equiv\alpha_{\mathrm{as}}-g_s-i\Delta k_0$, which depends on the linear response of the medium, and $Q\equiv\sqrt{q^2+4\kappa_s\kappa_{\mathrm{as}}}$. Note that α_{as}, g_s, κ_{as}, and κ_s are still functions of ϖ. Here we did not include the contribution from the Langevin operators. The reason is that we limit our discussion to a weak and far-detuned pumping and therefore the majority of the atomic population is in the ground state. In this case the contribution from Langevin noise operators to $B(\varpi)$ and $D(\varpi)$ is very small. This is confirmed by our numerical analysis. Please see the Appendix for a detailed discussion.

In the limit of low parametric gain where $4\kappa_s\kappa_{\mathrm{as}}\ll q^2$, Eqs. (49) and (50) reduce to

$$B(\varpi)=\frac{2\kappa_{\mathrm{as}}}{q[1+\coth(ql)]} \tag{51}$$

and

$$D(\varpi)=e^{(2g_s+i\Delta k_0)l}, \tag{52}$$

respectively. To make comparisons with the result in the interaction picture, we need to write q and g_s in terms of the Stokes and anti-Stokes wave numbers in the medium (k_s and k_{as}). The anti-Stokes wave number in the medium is $k_{\mathrm{as}}\approx\omega_{\mathrm{as}0}/c\ (1+\chi_{\mathrm{as}}/2)=k_{\mathrm{as}0}+\Delta k_{\mathrm{as}}$, with $\Delta k_{\mathrm{as}}\equiv\omega_{\mathrm{as}0}\chi_{\mathrm{as}}/(2c)$, and the Stokes wave number in the medium is $k_s\approx\omega_s/c\ (1+\chi_s/2)=k_{s0}+\Delta k_s$, with $\Delta k_s\equiv\omega_{s0}\chi_s/(2c)$. Then $q\approx-i(\Delta k_{\mathrm{as}}-\Delta k_s^{*}+\Delta k_0)$ and

$$B(\varpi)D^{*}(\varpi)=L\kappa_{\mathrm{as}}\mathrm{sinc}[(\Delta k_{\mathrm{as}}-\Delta k_s^{*}+\Delta k_0)l]\times e^{i(\Delta k_{\mathrm{as}}-\Delta k_s^{*}+2\Delta k_s)l}. \tag{53}$$

If the imaginary part of Δk_s is small, or the Raman gain is small, $\Delta k_s^{*}\approx\Delta k_s$. The product $B(\varpi)D^{*}(\varpi)$ becomes

$$B(\varpi)D^{*}(\varpi)=L\kappa_{\mathrm{as}}\mathrm{sinc}((\Delta k_{\mathrm{as}}-\Delta k_s+\Delta k_0)l)\times e^{i(\Delta k_{\mathrm{as}}+\Delta k_s)l}. \tag{54}$$

The argument inside the "sinc" function can be rewritten as $\Delta k_{\mathrm{as}}-\Delta k_s+\Delta k_0\equiv\Delta k$. The biphoton wave function is now

$$\psi(\tau)=-\frac{\omega_{\mathrm{as}0}}{i4\pi c}E_pE_cLe^{-i(k_{\mathrm{as}0}+k_{s0})L/2}\times\int d\varpi\,\chi^{(3)}_{\mathrm{as}}(\varpi)\mathrm{sinc}(\Delta kL/2)e^{i(k_{\mathrm{as}}+k_s)L/2}e^{-i\varpi\tau}, \tag{55}$$

which is consistent with the biphoton relative wave function in Eq. (19) in the interaction picture.

III. NUMERICAL RESULTS

We take the ^{85}Rb cold-atomic ensemble for numerical simulations. The relevant atomic energy levels involved are $|1\rangle=|5S_{1/2},F=2\rangle$, $|2\rangle=|5S_{1/2},F=3\rangle$, $|3\rangle=|5P_{1/2},F=3\rangle$, and $|4\rangle=|5P_{3/2},F=3\rangle$. The pump laser is detuned by $\Delta_p=2\pi\times 150$ MHz. The atomic medium has a length $L=2$ cm.

We work in the ground-state approximation where the field of the pump laser is weak and far detuned from the $|1\rangle\rightarrow|4\rangle$ transition so that most of the atomic population is in the ground state. The linear and third-order susceptibilities of the Stokes

and anti-Stokes fields are [21,28,29]

$$\chi_s(z,\omega_{s0}-\varpi) = \frac{N(z)|\mu_{24}|^2|\Omega_p(z)|^2(\varpi-i\gamma_{13})/(\varepsilon_0\hbar)}{(\Delta_p^2+\gamma_{14}^2)[|\Omega_c(z)|^2-4(\varpi-i\gamma_{12})(\varpi-i\gamma_{13})]}, \tag{56}$$

$$\chi_{\rm as}(z,\omega_{\rm as0}+\varpi) = \frac{4N(z)|\mu_{13}|^2(\varpi+i\gamma_{12})/(\varepsilon_0\hbar)}{|\Omega_c(z)|^2-4(\varpi+i\gamma_{12})(\varpi+i\gamma_{13})}, \tag{57}$$

$$\chi_s^{(3)}(z,\omega_{s0}-\varpi) = \frac{N(z)\mu_{13}\mu_{24}\mu_{14}^*\mu_{23}^*/(\varepsilon_0\hbar^3)}{(\Delta_p+i\gamma_{14})[|\Omega_c(z)|^2-4(\varpi-i\gamma_{12})(\varpi-i\gamma_{13})]}, \tag{58}$$

$$\chi_{\rm as}^{(3)}(z,\omega_{\rm as0}+\varpi) = \frac{N(z)\mu_{13}\mu_{24}\mu_{14}^*\mu_{23}^*/(\varepsilon_0\hbar^3)}{(\Delta_p+i\gamma_{14})[|\Omega_c(z)|^2-4(\varpi+i\gamma_{12})(\varpi+i\gamma_{13})]}. \tag{59}$$

Here, $N(z)=N_0 f_N(z)$ is the MOT atomic density, μ_{ij} is the dipole moment for the $|i\rangle$ to $|j\rangle$ transition, $\Omega_p(z)=\Omega_p f_p(z)=\mu_{41}E_p(z)/\hbar$ is the Rabi frequency of the pump laser field, and $\Omega_c(z)=\Omega_c f_c(z)=\mu_{32}E_c(z)/\hbar$ is the Rabi frequency of the coupling laser field. γ_{ij} is the dephasing rate between $|i\rangle$ and $|j\rangle$. As the natural linewidth of ^{85}Rb atoms is $\Gamma=2\pi\times 6$ MHz, we have $\gamma_{13}=\gamma_{14}=\gamma_{23}=\Gamma/2$. For simulation, we take the ground-state dephasing rate $\gamma_{12}=0.01\gamma_{13}$. Other parameters are ${\rm OD}=N_0\sigma_{13}L=150$, $\Omega_p=2\pi\times 1.2$ MHz, and $\Omega_c=2\pi\times 12$ MHz, unless they are specified.

Note that in calculating the Stokes–anti-Stokes biphoton wave function in the interaction picture, we take $\chi^{(3)}(\varpi)=\chi_{\rm as}^{(3)}(\omega_{\rm as0}+\varpi)=\chi_s^{(3)}(\omega_{s0}+\varpi)$.

A. Photon properties

In Sec. II B, we proved that both the interaction and the Heisenberg pictures give the same biphoton waveform, characterized by $\psi(\tau)$ when there is no z dependence of the atomic density and the driving laser fields. The biphoton waveform is determined by two parts, $F(\varpi)$ and $Q(\varpi)$. $F(\varpi)$ involves the nonlinear response $\chi^{(3)}$ and the phase-mismatching effect, while $Q(\varpi)$ implies the linear propagation effect in the atomic medium. In the expression of $\chi^{(3)}$, the term $[|\Omega_c(z)|^2-4(\varpi+i\gamma_{12})(\varpi+i\gamma_{13})]$ in the denominator can be rewritten as $(-1/4)[(\varpi-\Omega_e/2+i\gamma_e)(\varpi+\Omega_e/2+i\gamma_e)]$, where $\Omega_e\equiv\sqrt{|\Omega_c|^2-(\gamma_{13}-\gamma_{12})^2}$ is the effective Rabi frequency, and $\gamma_e\equiv(\gamma_{12}+\gamma_{13})/2$ is the effective dephasing rate. It can be seen from the rewritten term that there are two resonances, $\varpi=\pm\Omega_e/2$, with the linewidth determined by $2\gamma_e$. Inside $F(\varpi)$, there is also the term $\mathrm{sinc}(\Delta kL/2)$, and its bandwidth is determined by the group delay time, τ_g, as $\Delta\omega_g\equiv(2\pi\times 0.88)/\tau_g$; here $\tau_g=L/V_g\simeq(2\gamma_{13}{\rm OD})/|\Omega_c|^2$ [25]. Using our simulation parameters, $\tau_g=970$ ns. For $Q(\varpi)$, which determines the EIT transmission, its bandwidth can be calculated from Eqs. (56) and (57). The effective value is 1.62 MHz with the same parameters. It gives $\Delta\omega_{\rm tr}\simeq|\Omega_c|^2/(2\gamma_{13}\sqrt{\rm OD})$.

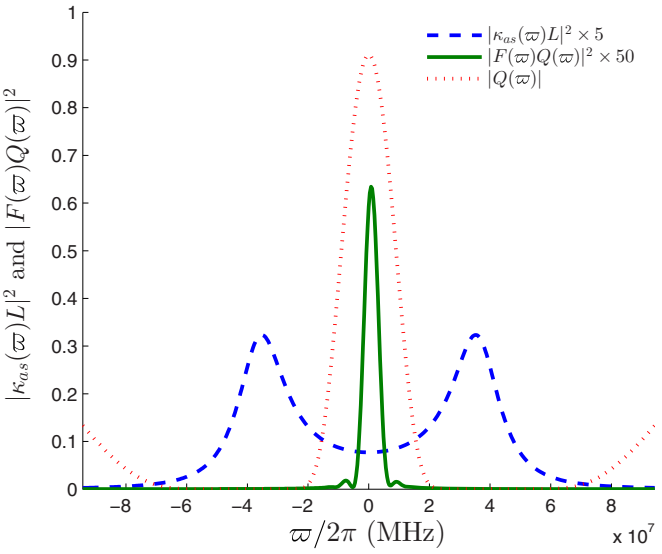

FIG. 2. $|\kappa_{\rm as}(\varpi)L|^2$, $Q(\varpi)$, and two-photon spectrum $|F(\varpi)Q(\varpi)|^2$ vs the varying component of the frequency of the anti-Stokes field ϖ. Note that $|\kappa_{\rm as}(\varpi)L|^2$ is magnified 5 times and $|F(\varpi)Q(\varpi)|^2$ is magnified 50 times here.

When $(\Omega_e,2\gamma_e)<(\Delta\omega_g,\Delta\omega_{\rm tr})$, the system is in the damped Rabi oscillation regime. This happens when $|\Omega_c|$ is large and the OD is small. The biphoton waveform is determined by the two resonances of the third-order response. When the OD is large (typically ${\rm OD}\geqslant 4\pi^2$), we may have $\Omega_e>\Delta\omega_{\rm tr}>\Delta\omega_g$. Then the two resonances are suppressed by the phase mismatching $\mathrm{sinc}(\Delta kL/2)$ and the off-resonance EIT absorption. In this case, the phase-mismatching term sets the limit of the bandwidth of the biphotons and the group delay time is related to the biphoton correlation time. This is the group delay regime.

In Fig. 2, we plot $|\kappa_{\rm as}(\varpi)\times L|^2$, $|Q(\varpi)|$, and $|F(\varpi)\times Q(\varpi)|^2$ as a function of ϖ. The function $|\kappa_{\rm as}(\varpi)\times L|^2$ has two peaks, which are far detuned from the central frequency of $|F(\varpi)\times Q(\varpi)|^2$ and $|Q(\varpi)|$. Note that $\kappa_{\rm as}(\varpi)$ is given in Eq. (35) and is proportional to $\chi^{(3)}$. Note also that as the $\mathrm{sinc}(\Delta kL/2)$ function has the same spectrum as $|F(\varpi)\times Q(\varpi)|^2$, it is not plotted in the figure. It is clear that Fig. 2 lies in the group delay regime. In this paper, we limit our discussion to the group delay regime.

When the parametric gain is small as in our case, the Stokes and anti-Stokes are generated spontaneously in pairs. The multimode chaotic nature is verified by their second-order coherence, shown in Fig. 3 as the normalized autocorrelation functions obtained in the Heisenberg picture: $g_{s,s}^{(2)}(0)=g_{\rm as,as}^{(2)}(0)=2$, and $1\leqslant g_{\rm as,as}^{(2)}(\tau)\leqslant 2$ as well as $1\leqslant g_{s,s}^{(2)}(\tau)\leqslant 2$.

The normalized cross-correlation $g_{s,\rm as}^{(2)}(\tau)$ in Fig. 4 shows a rectangular shape. The correlation time is nearly 1 μs, which is determined by the bandwidth of the biphoton spectrum $|F(\varpi)\times Q(\varpi)|^2$ in Fig. 2.

To determine the properties of the generated biphotons, we calculate the ratio of the normalized cross-correlation function to the normalized autocorrelation function $[g_{s,\rm as}^{(2)}(\tau)]^2/[g_{s,s}^{(2)}(0)g_{\rm as,as}^{(2)}(0)]$. As shown in Fig. 5, the Cauchy-Schwarz inequality is violated by a factor of about 4200 and the biphoton nonclassical property is clearly confirmed.

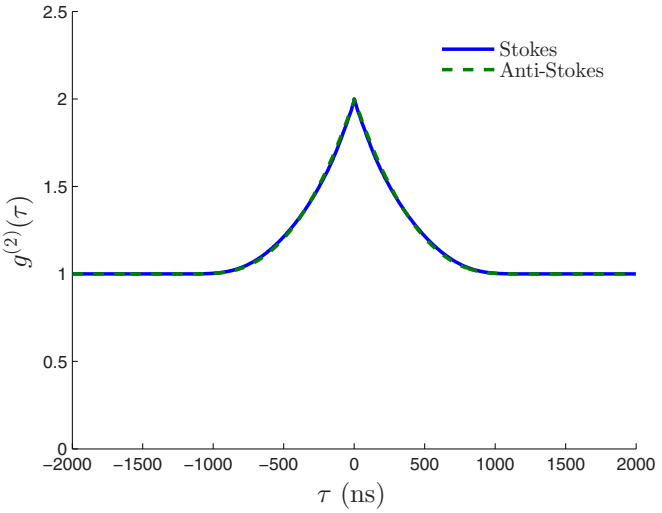

FIG. 3. Normalized autocorrelation functions $g^{(2)}_{s,s}(\tau)$ and $g^{(2)}_{\mathrm{as,as}}(\tau)$ calculated in the Heisenberg picture. No z dependence of the atomic density or the driving laser fields.

Next, as we increase the pump power to increase the photon generation rate, the parametric gain increases, but the factor of violation of the Cauchy-Schwarz inequality decreases, as shown in Fig. 6.

Note that because the perturbation theory in the interaction picture describes only the two-photon process, the single-photon generation rates R_s and R_{as} in the interaction picture cannot be described adequately by the biphoton state. As such, we obtain the normalized cross- and autocorrelation functions $g^{(2)}_{s,\mathrm{as}}(\tau)$, $g^{(2)}_{s,s}(\tau)$, and $g^{(2)}_{\mathrm{as,as}}(\tau)$ in the Heisenberg picture.

B. Comparison of the two formalisms

We compare the two models in the interaction and Heisenberg pictures by computing the second-order Glauber function $G^{(2)}_{s,\mathrm{as}}(\tau)$ numerically for cases with and without z dependence

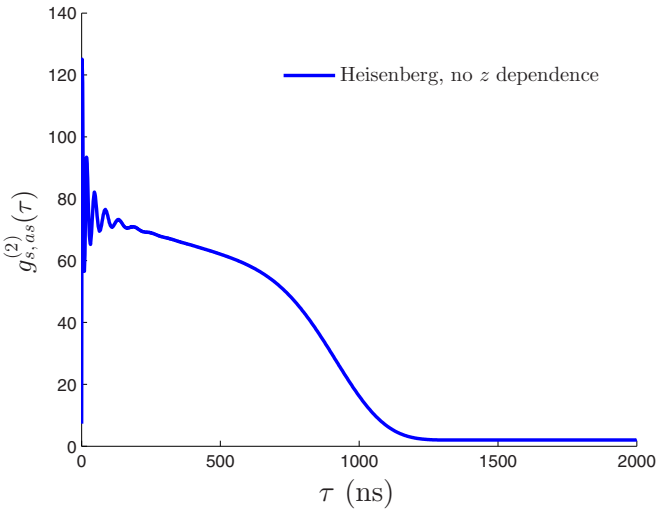

FIG. 4. Normalized cross-correlation function $g^{(2)}_{s,\mathrm{as}}(\tau)$ calculated in the Heisenberg picture. No z dependence of the atomic density or the driving laser fields.

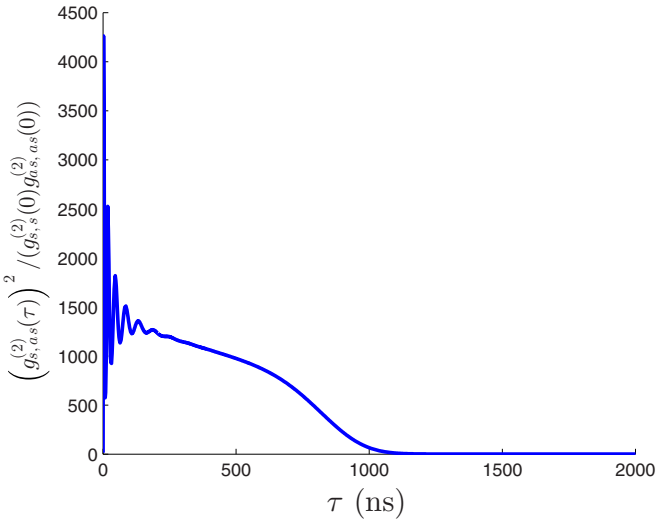

FIG. 5. Ratio of the normalized cross-correlation function to the normalized autocorrelation function $(g^{(2)}_{s,\mathrm{as}}(\tau))^2/(g^{(2)}_{s,s}(0)g^{(2)}_{\mathrm{as,as}}(0))$ calculated in the Heisenberg picture. No z dependence of the atomic density or the driving laser fields.

in the atomic density and the driving laser fields. We have shown theoretically that when there is no z dependence in the atomic density or the driving field intensities the two models agree well when $q^2 \gg 4\kappa_s\kappa_{\mathrm{as}}$ or when the linear response is much larger than the third-order response in the atomic medium. This is the low-parametric-gain regime. In the subsequent figures, we show numerically that the two models agree well in this regime when spatial dependence is absent or present in the the atomic density and driving laser fields.

Figure 7 shows that with a uniformly distributed atomic density and uniform pump and coupling field amplitudes in the z direction, the two models agree well in predicting the

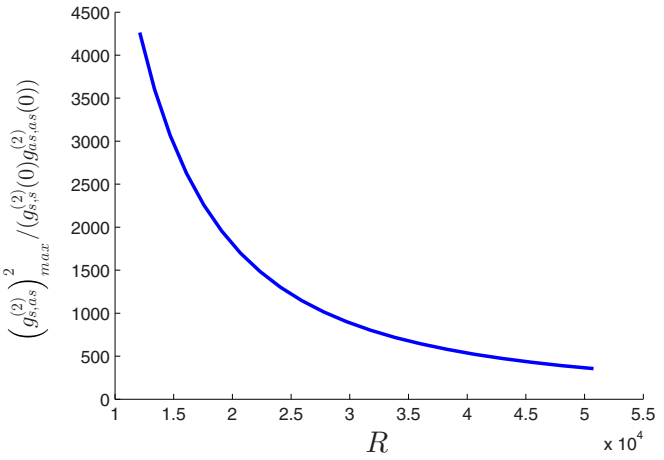

FIG. 6. Ratio of the normalized cross-correlation function to the normalized autocorrelation function $(g^{(2)}_{s,\mathrm{as}})^2_{\mathrm{max}}/(g^{(2)}_{s,s}(0)g^{(2)}_{\mathrm{as,as}}(0))$ vs the photon pair emission rate R calculated in the Heisenberg picture as the pump power is doubled. No z dependence of the atomic density or the driving laser fields. The normalized cross-correlation function $g^{(2)}_{s,\mathrm{as}}$ is taken at its maximum value.

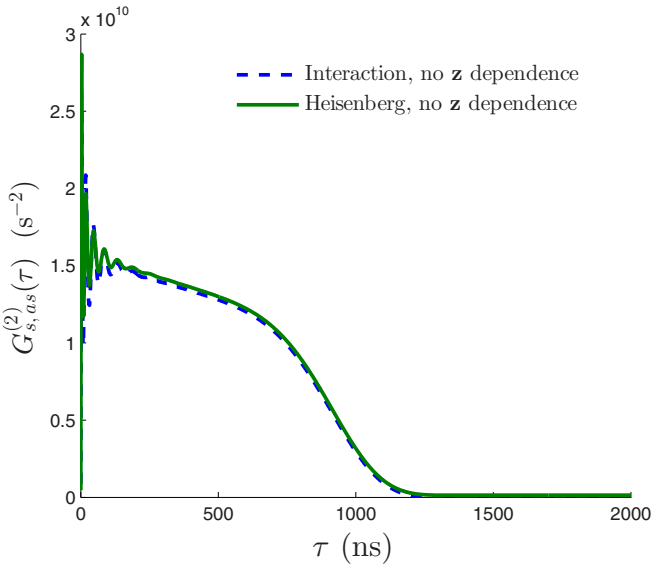

FIG. 7. $G^{(2)}_{s,\mathrm{as}}(\tau)$ in both the interaction and the Heisenberg pictures for a uniform atomic medium and uniform pump and coupling laser profiles in the z direction.

second-order Glauber function $G^{(2)}_{s,\mathrm{as}}(\tau)$. The curves are rectangle-like with an oscillatory optical precursor.

Next we look at the case where the atomic density is not uniform in the z direction but is modulated in such a way that the total OD is unchanged; i.e., the modulation function $f_N(z)$ satisfies $\int_{-L/2}^{L/2} f_N(z)dz = L$. Figure 8 shows that both models produce the same numerical results.

In Fig. 9, we give a Gaussian profile to the pump or coupling laser such that $E_p(z) = E_p f_p(z)$ or $E_c(z) = E_c f_c(z)$, with $f_p(z) = f_c(z) = 1/0.65\exp(-z^2/(L/2)^2)$. Both models produce the same $G^{(2)}_{s,\mathrm{as}}(\tau)$. Note that the shape is very different from those in Figs. 7 and 8. Here the waveform is not

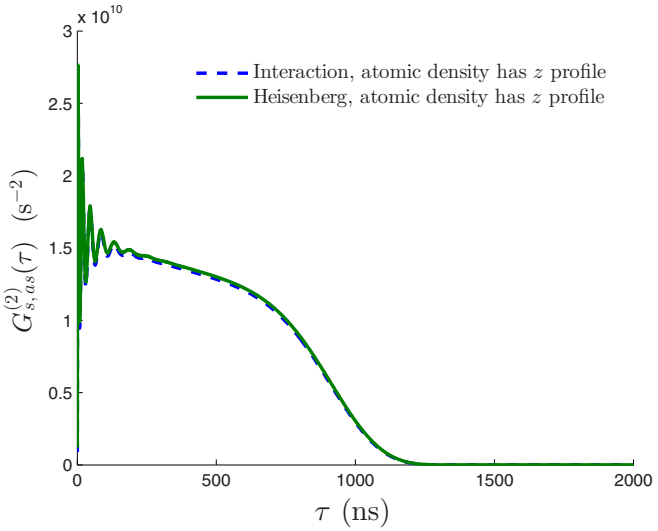

FIG. 8. $G^{(2)}_{s,\mathrm{as}}(\tau)$ in both the interaction and the Heisenberg pictures for uniform pump and coupling laser profiles in the z direction; the atomic density is nonuniform with modulation function $f_N(z) = 6(z + L/2)(L/2 - z)/L^2$.

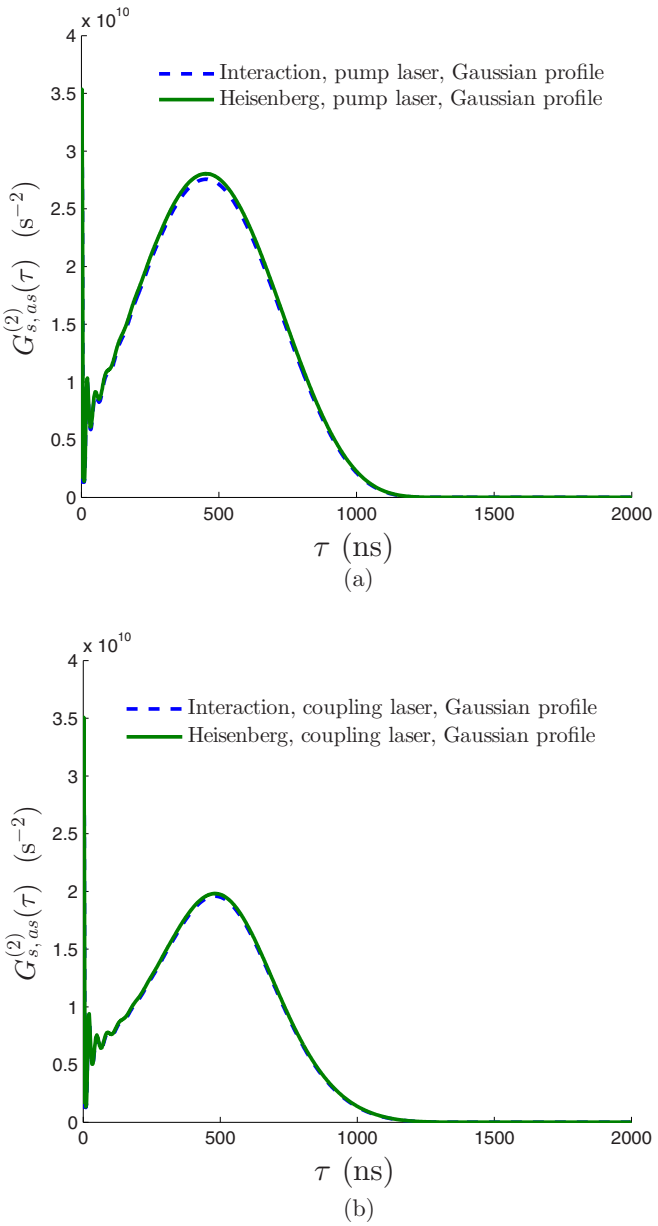

FIG. 9. $G^{(2)}_{s,\mathrm{as}}(\tau)$ in both the interaction and the Heisenberg pictures for a uniform atom density: (a) only the pump laser has a Gaussian profile in the z direction; (b) only the coupling laser has a Gaussian profile in the z direction. The Gaussian modulation function is $f_{p,c}(z) = 1/0.65\exp(-z^2/(L/2)^2)$.

rectangle-like but Gaussian-like, with a huge bump in the middle. This is a result of Eq. (30), where the space-domain modulating function $f_p(z)$ determines the shape of the time-domain waveform. As discussed in Fig. 2, in the group delay regime, the third-order susceptibility is almost a constant in the biphoton frequency detuning window. When the atomic density (or OD) is high, the value of $\chi^{(3)}$ is large, and the effect of modulation caused by the driving field profile is more significant. Therefore this Gaussian-like waveform was not observed for small ODs. It is also demonstrated that the peak of the waveform is higher in Fig. 9(a) than in Fig. 9(b). This shows that the effect of the mapping from the space domain to the time domain is more pronounced when the pump laser

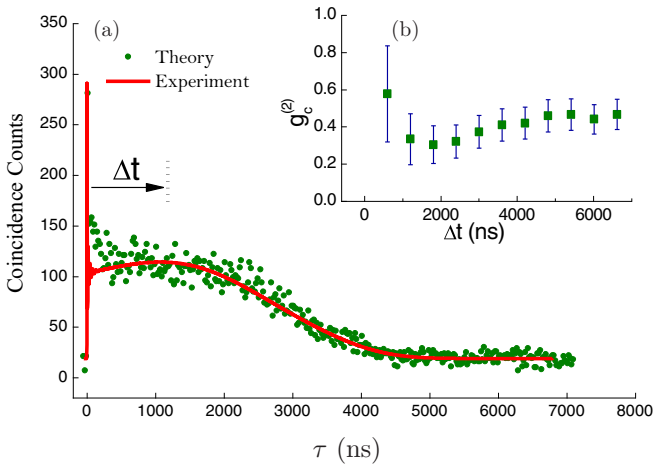

FIG. 10. (a) Probe laser EIT transmission spectrum. (b) Two-photon coincidence counts collected over 3600 s as a function of the relative time delay. Operating parameters are OD = 175, $\Omega_c = 2\pi \times 5.82$ MHz, and $\Omega_p = 2\pi \times 0.47$ MHz. (c) Measured conditional autocorrelation $g_c^{(2)}$ of heralded anti-Stokes photons as a function of the coincidence window width Δt.

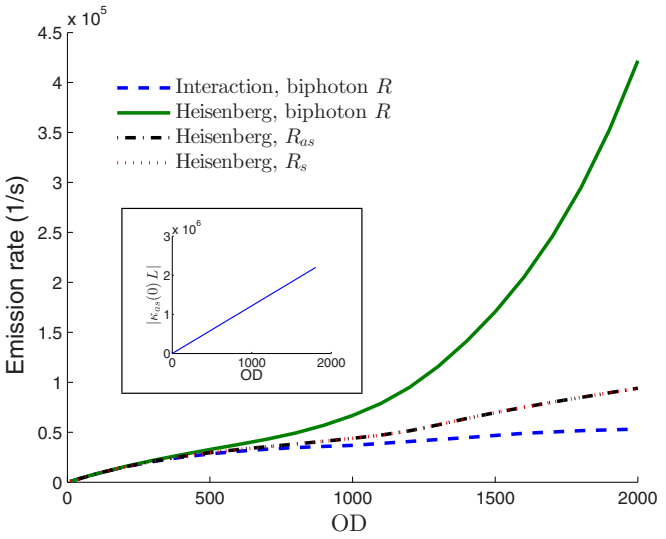

FIG. 11. Comparison of the biphoton generation rate in the interaction (dashed line) and Heisenberg (solid line) pictures as the OD increases from 100 to 300 upon increasing the atomic density. The x axis is the product of $|\kappa_{\rm as}(\varpi = 0)\,L|$. Inset: This quantity varies linearly with the OD.

has a z profile. This is because in the third-order susceptibility [Eq. (59)], when the coupling laser has a z profile $f_c(z)$, it appears in the denominator of $\chi^{(3)}$ through $\Omega_c(z)$. Larger values of $f_c(z)$ result in smaller $\chi^{(3)}$ and, thus, smaller $\psi(\tau)$ [Eq. (30)].

The Gaussian-like biphoton waveform was observed in experiments for the first time by Zhao *et al.* [12] and was fitted well by a Gaussian modulation to the pump field. Following the experimental configuration described in [12], we attempt to explore biphotons with a longer coherence time and narrower bandwidth. Working in the group delay regime, we have achieved a significant improvement in the generation of narrowband biphotons with a long coherence time by optimizing the OD (OD = 175) while keeping the low atomic ground-state dephasing rate ($\gamma_{12} = 2\pi \times 30$ KHz). The peak values of the coupling and pump laser Rabi frequency are $\Omega_c = 2\pi \times 5.82$ MHz and $\Omega_p = 2\pi \times 0.47$ MHz. Here we use a less modulated pump and coupling field [$f_p(z) = f_c(z) = 1/0.9\exp(-z^2/(L/2)^2)$]. As shown in Fig. 10(a), the green circles are the biphoton coincidence counts collected in 3600 s, and the red curve is the theoretical calculation $\eta G^{(2)}_{s,\rm as}(\tau)\Delta t_{\rm bin} T$, where $\eta = 0.5\%$ includes the joint-detection efficiency (5%) and the duty cycle (10%), $\Delta t_{\rm bin} = 10$ ns is the time bin width, and T is the collecting time. From Fig. 10(a), the biphoton $1/e$ correlation time is 3280 ns. To verify the quantum particle nature of heralded single photons, we measure the conditional second-order autocorrelation of anti-Stokes photons. We use the Stokes photons as the gates, send the anti-Stokes photons to a beam splitter, and measure the two outputs by two SPCMs. The conditional autocorrelation is calculated by $g_c^{(2)} = (N_s N_{s12}/N_{s1}N_{s2})$, where N_s is the Stokes counts, N_{s1} and N_{s2} are the twofold coincidence counts, and N_{s12} is the threefold coincidence counts. We can use the value of $g_c^{(2)}$ to characterize the photon property. Note that a coherent state, two-photon Fock state, and single-photon state give $g_c^{(2)} = 1$, 0.5, and 0, respectively [34]. Figure 10(b) shows the measured $g_c^{(2)}$ of anti-Stokes photons, from which we can confirm the heralded single-photon property of anti-Stokes photons.

So far, we have shown that when there is no z dependence of the atomic density or the driving laser field intensities the two models agree well when $q^2 \ll 4\kappa_s\kappa_{\rm as}$, or when the linear response is much larger than the third-order response in the atomic medium. The numerical plots even for a nonuniform atomic density and nonuniform driving laser profiles agree as well. Now the questions are: What happens when q^2 is no longer much larger than $4\kappa_s\kappa_{\rm as}$, and In what region of the parameter space do they differ? To answer these questions, we plot the photon pair generation rate as a function of $|\kappa_{\rm as}(\varpi = 0)\,L|$ by varying the OD from 100 to 300. We consider a homogeneous atomic cloud and uniform laser fields. Figure 11 shows that in the small-parametric-gain regime where $|\kappa_{\rm as}(\varpi = 0)\,L|$ is small, both models predict the same biphoton rate. However, in the large-parametric-gain regime where $|\kappa_{\rm as}(\varpi = 0)\,L|$ is large and $q^2 \ll 4\kappa_s\kappa_{\rm as}$ no longer holds, the biphoton rate is higher in the Heisenberg picture.

When the third-order response is small, the two-photon process dominates. This can be described adequately by the first-order perturbation approximation in the interaction picture. For large $|\kappa_{\rm as}(\varpi = 0)\,L|$, apart from the two-photon process, n-photon ($n > 2$) processes are present; this is included in the Heisenberg formalism but not in the interaction formalism. This is because the first-order perturbation approximation describes only the biphoton process. Therefore, for comparisons with experimental data in the large-parametric-gain regime, the Heisenberg picture should be used. Note that in Figs. 7, 8, and 9, $|\kappa_{\rm as}(\varpi = 0)\,L| = 0.115$. Therefore, we can use either model where the biphoton process dominates and the n-photon ($n > 2$) processes are negligible. Note also that in the group delay regime, the biphoton joint spectrum is determined by the phase-matching condition. As shown in Fig. 2, the phase-matching spectrum function $|F(\varpi)Q(\varpi)|$ is much narrower than the nonlinear gain spectrum $|\kappa_{\rm as}(\varpi)\,L|$.

Therefore, we choose $|\kappa_{\rm as}(\varpi = 0)\, L|$ as a (dimensionless) parameter to compare the biphoton generation rate in Fig. 11.

IV. QUANTUM WAVEFORM SHAPING AND ENGINEERING

In this section, we explore the possibilities of manipulating the biphoton temporal waveform by tailoring the pump laser spatial profiles. We keep the atomic density and the coupling laser profile uniform in space. Figure 12(a) shows a pump laser with three z profiles: (i) a full Gaussian function, $f_p(z) = 1/0.65\exp(-z^2/(L/2)^2)$, and (ii, iii) a half-Gaussian profile, with either the left or the right side of the beam covered from the center of the Gaussian curve. This means that only half of the atomic cloud is exposed to the pump laser. The corresponding $G^{(2)}_{s,\rm as}(\tau)$ is plotted in Fig. 12(b). It is expected that when half of the laser beam is covered, $G^{(2)}_{s,\rm as}(\tau)$ should be lower than when the full beam is present. However, it is interesting that when the MOT that lies in $(0, L/2)$ is exposed to the half-Gaussian beam, the nonzero part of $G^{(2)}_{s,\rm as}(\tau)$ in the space domain is shifted to the longer-delay part of the time domain, and vice versa. This is explained in Sec. II A 3.

Next, we block the center part of the Gaussian beam; i.e., the part of the atomic cloud that lies in $(L/3, 2L/3)$ is not subjected to the pump laser beam [Fig. 13(a)]. $G^{(2)}_{s,\rm as}(\tau)$ is shown in Fig. 13(b). There are two bumps present, corresponding to the two parts of the pump laser profile, as well as the biphoton

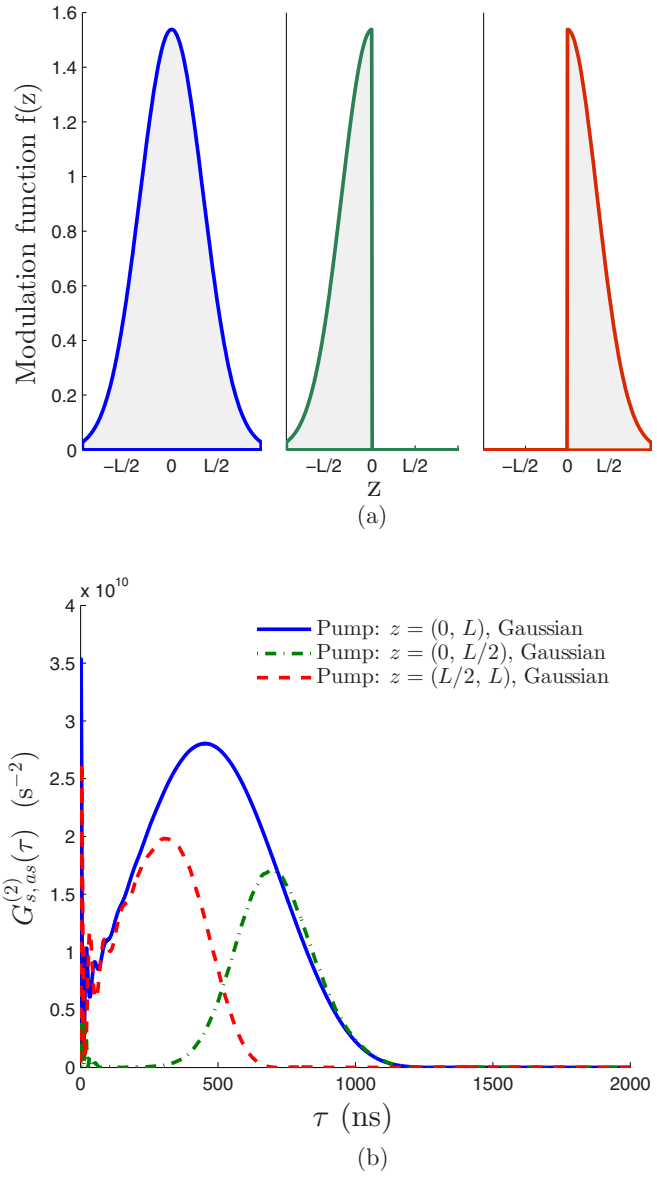

FIG. 12. (a) The z profile of the pump laser varies from a full Gaussian function, $f(z) = 1/0.65\exp(-z^2/(L/2)^2)$, to two half-Gaussian functions, $f_l(z) = 1/0.65\exp(-z^2/(L/2)^2)$ for $0 < z < L/2$ and 0 for $L/2 < z < L$, $f_r(z) = 0$ for $0 < z < L/2$ and $f_r(z) = 1/0.65\exp(-z^2/(L/2)^2)$ for $L/2 < z < L$. (b) $G^{(2)}_{s,\rm as}(\tau)$ corresponding to the pump laser profile as a full-Gaussian $f(z)$, a half blocked Gaussian $f_l(z)$, and another half-blocked Gaussian $f_r(z)$.

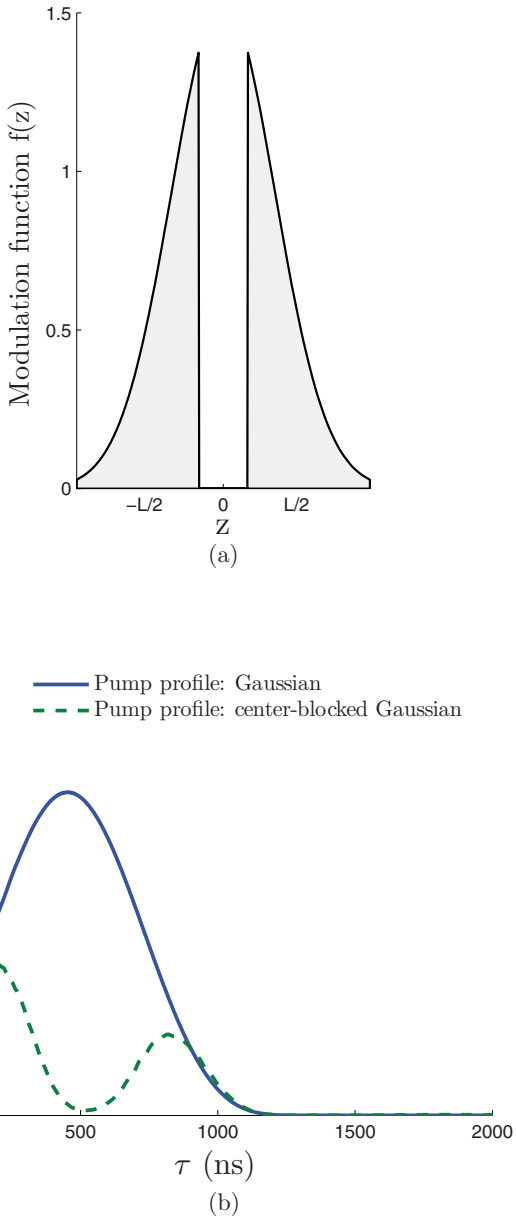

FIG. 13. (a) The z profile of the pump laser varies from a center-blocked Gaussian function, $f_p(z) = 1/0.65\exp(-z^2/(L/2)^2)$ for $z < L/3$ and $z > 2L/3$, and 0 otherwise. (b) The corresponding $G^{(2)}_{s,\rm as}(\tau)$ for the blocked and full Gaussian profiles.

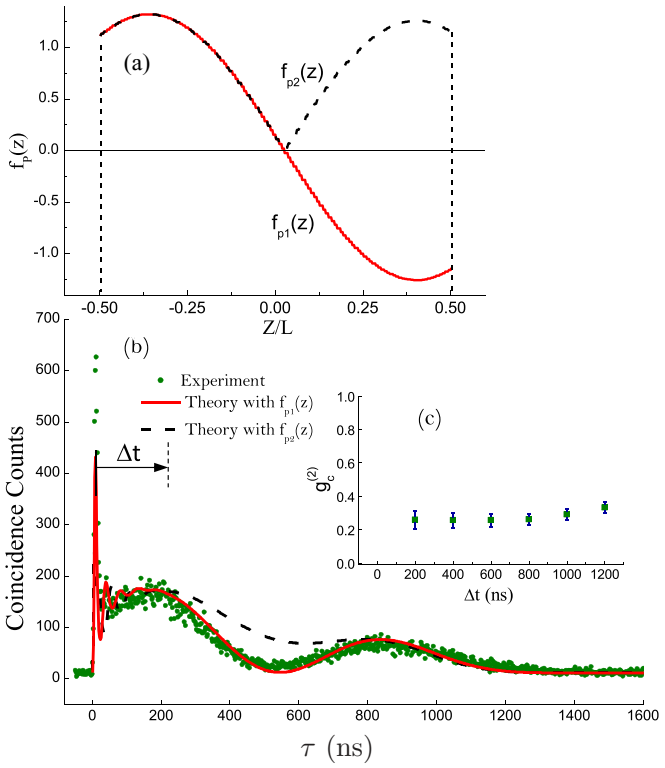

FIG. 14. Shaping biphoton temporal waveform with double peaks. (a) Pump laser spatial profile along z. (b) Coincidence counts collected in 3000 s, and theoretical biphoton waveforms. (c) Measured $g_c^{(2)}$ of heralded single anti-Stokes photons. Data are taken from [35].

optical precursor. For comparison, we also show the case where the pump laser has a full Gaussian profile.

From Eq. (31), we can see that the spatial profile of the pump laser is mapped to the temporal biphoton waveform; meanwhile there is always a decay tail on the biphoton waveform, which stems from the slowly propagating anti-Stoke photons. To achieve a biphoton waveform with two separate bumps, the two parts of the pump laser profile in the longitudinal direction require a large separation as shown in Fig. 13(a). Another way to get a waveform with two bumps is to modulate the phase of the pump light [35]. In Fig. 14(a), the solid red curve shows the pump laser spatial light along z, with the first and second halves carrying opposite phases. The experimental data on the corresponding biphoton coincidence counts are represented by the green circles in Fig. 14(b). The solid red curve in Fig. 14(b) shows the theoretical calculation taking into account the phase of the pump laser. For comparison, we also show the result for pumps with a uniform phase curve in Figs. 14(a) and 14(b). Figure 14(c) shows the measured conditional autocorrelation of heralded anti-Stokes photons. The value is well below 0.5, which is clear evidence of the quantum nature of heralded single photons for anti-Stokes photons.

Note that another method of biphoton waveform shaping is via modulation of the temporal profiles of the driving laser fields [19,20]. Compared to this method, the spatial modulation method maintains a perfect frequency entanglement (frequency anticorrelation) due to energy conservation raised from the time translation symmetry, while the temporal modulation reduces the frequency entanglement because of the breakdown of the time translation symmetry. However, the temporal-to-temporal shaping is much easier to implement with a larger modulation bandwidth compared to the spatial-to-temporal mapping. Therefore, when a perfect frequency anticorrelation is more important to applications, the spatial modulation technique should be the choice.

In general, if we can control the profile of the driving laser fields spatially, we can produce interesting biphoton waveforms temporally. These interesting waveforms might open up more applications in quantum information technology. For example, information on the spatial pattern of the driving fields can be coded into the temporal pattern of the biphoton waveform. On the other hand, a time-domain biphoton waveform allows us to deduce the information on the space-domain profile of the driving lasers, so a desired time-domain pattern can be obtained with corresponding modulations of the laser profiles in the space domain.

V. CONCLUSIONS

We have generalized and compared the theoretical modeling of biphoton generation through the SFWM process. We show that both approaches, in the interaction and Heisenberg pictures, agree well in the low-parametric-gain regime. Moreover, when the pump and coupling lasers have a nonuniform profile in the atomic medium, the second-order correlation function of Stokes–anti-Stokes is no longer rectangle-like with a modified exponential tail, but Gaussian-like with a peak in the middle. This is confirmed by recent experimental data. We also predict that one can control the shape of the time-domain biphoton waveform by tailoring the space-domain profile of the pump and coupling lasers, especially the pump profile, as it dominates the effect from space-to-time mapping.

ACKNOWLEDGMENT

This work was supported by the Hong Kong Research Grants Council (Project No. 601113).

APPENDIX: SOLUTION TO THE COUPLED EQUATIONS IN THE HEISENBERG-LANGEVIN FORMALISM

As the susceptibilities are functions of ϖ, $\alpha_{\rm as}$, g_s, $\kappa_{\rm as}$, and κ_s are also functions of ϖ. The general solution to (34) at $z = l$ can be written as

$$\begin{pmatrix} \hat{a}_{\rm as}(l,\varpi) \\ \hat{a}_s^\dagger(l,-\varpi) \end{pmatrix} = \begin{pmatrix} A_1(\varpi) & B_1(\varpi) \\ C_1(\varpi) & D_1(\varpi) \end{pmatrix} \begin{pmatrix} \hat{a}_{\rm as}(-l,\varpi) \\ \hat{a}_s^\dagger(-l,-\varpi) \end{pmatrix} + \sum_{\alpha_i} \int_{-l}^{l} dz\, e^{M(z-l)} \begin{pmatrix} \beta_{\alpha_i}^{\rm as} \\ \beta_{\alpha_i}^{s} \end{pmatrix} \hat{f}_{\alpha_i}^\dagger. \quad \text{(A1)}$$

where the transform matrix can be obtained by numerically solving the coupled equation by setting the Langevin forces to 0. M is given by

$$M = \begin{pmatrix} \alpha_{\rm as}(z,\varpi) - i\frac{\Delta k_0}{2} & -\kappa_{\rm as}(z,\varpi) \\ -\kappa_s(z,\varpi) & g_s(z,\varpi) + i\frac{\Delta k_0}{2} \end{pmatrix}. \quad \text{(A2)}$$

Equation (A1) can be rewritten as Eq. (39), where

$$\begin{aligned} A(\varpi) &= A_1(\varpi) - \frac{B_1(\varpi)C_1(\varpi)}{D_1(\varpi)}, \\ B(\varpi) &= \frac{B_1(\varpi)}{D_1(\varpi)}, \\ C(\varpi) &= -\frac{C_1(\varpi)}{D_1(\varpi)}, \\ D(\varpi) &= \frac{1}{D_1(\varpi)}, \end{aligned} \tag{A3}$$

and

$$\begin{pmatrix} P_{\alpha_i} \\ Q_{\alpha_i} \end{pmatrix} = \begin{pmatrix} 1 & -\frac{B_1(\varpi)}{D_1(\varpi)} \\ 0 & -\frac{1}{D_1(\varpi)} \end{pmatrix} e^{M(z-L)} \begin{pmatrix} \beta^{\rm as}_{\alpha_i} \\ \beta^{s}_{\alpha_i} \end{pmatrix}. \tag{A4}$$

The two-photon correlation Glauber function is given by

$$\begin{aligned} G^{(2)}_{s,\rm as}(t,t+\tau) &= \langle \hat{a}^\dagger_{\rm as}(l,t+\tau)\hat{a}^\dagger_s(-l,t)\hat{a}_s(-l,t)\hat{a}_{\rm as}(l,t+\tau)\rangle \\ &= \frac{1}{(2\pi)^2}\int d\varpi_1 d\varpi_2 d\varpi_3 d\varpi_4 e^{i\varpi_1(t+\tau)-i\varpi_2 t+i\varpi_3 t-i\varpi_4(t+\tau)}\langle \hat{a}^\dagger_{\rm as}(l,\varpi_1)\hat{a}^\dagger_s(-l,-\varpi_2)\hat{a}_s(-l,-\varpi_3)\hat{a}_{\rm as}(l,\varpi_4)\rangle. \end{aligned} \tag{A5}$$

From Eq. (39) and the boundary condition [Eq. (38)], assuming the starting time $t = 0$, the Glauber function is then

$$G^{(2)}_{s,\rm as}(\tau) = \left| \int \frac{d\varpi}{2\pi} e^{-i\varpi\tau} \left[B(\varpi)D^*(\varpi) + \sum_{\alpha_i,\alpha_j} \int_{-l}^{l} dz\, Q^*_{\alpha_i} D_{\alpha_i,\alpha_j^\dagger} P_{\alpha_j} \right] \right|^2 + R_{\rm as} R_s. \tag{A6}$$

The second term in (A6) is the product of the Stokes and anti-Stokes generation rates, R_s and $R_{\rm as}$. This term describes a uniform background.

The Langevin noise coefficients are given by

$$\beta^{\rm as}_{21} = -\frac{\sqrt{2}\,\Omega_c(z)\sqrt{N(z)\sigma_{13}\gamma_{13}}}{G(\varpi)}, \tag{A7}$$

$$\beta^{\rm as}_{24} = \left(\frac{\Omega_p(z)}{\Delta_p}\right)\frac{\Omega_c(z)\sqrt{N(z)\sigma_{13}\gamma_{13}}}{\sqrt{2}\,G(\varpi)}, \tag{A8}$$

$$\beta^{\rm as}_{31} = \frac{2\sqrt{2}\,(\varpi + i\gamma_{12})\sqrt{N(z)\sigma_{13}\gamma_{13}}}{G(\varpi)}, \tag{A9}$$

$$\beta^{\rm as}_{34} = -\left(\frac{\Omega_p(z)}{\Delta_p}\right)\frac{\sqrt{2}\,(\varpi + i\gamma_{12})\sqrt{N(z)\sigma_{13}\gamma_{13}}}{G(\varpi)}, \tag{A10}$$

$$\beta^{s}_{21} = -\left(\frac{\Omega_p(z)}{\Delta_p}\right)\frac{\sqrt{2}\,(\varpi + i\gamma_{13})\sqrt{N(z)\sigma_{24}\gamma_{24}}}{G(\varpi)}, \tag{A11}$$

$$\beta^{s}_{24} = \frac{\sqrt{N(z)\sigma_{24}\gamma_{24}}}{\sqrt{2}\,\Delta_p}, \tag{A12}$$

$$\beta^{s}_{31} = \left(\frac{\Omega_p(z)}{\Delta_p}\right)\frac{\Omega_c(z)\sqrt{N(z)\sigma_{24}\gamma_{24}}}{\sqrt{2}\,G(\varpi)}, \tag{A13}$$

$$\beta^{s}_{34} = \frac{\Omega_c(z)\sqrt{N(z)\sigma_{24}\gamma_{24}}}{2\sqrt{2}\,\Delta_p^2}. \tag{A14}$$

Here $G(\varpi) \equiv |\Omega_c(z)|^2 - 4(\varpi + i\gamma_{12})(\varpi + i\gamma_{13})$ and σ_{ij} is the absorption cross section for the $|j\rangle \to |i\rangle$ transition. γ_{ij} is the dephasing rate between $|i\rangle$ and $|j\rangle$.

The diffusion coefficients are given by

$$D_{\alpha_i,\alpha_j^\dagger} = \begin{pmatrix} 2\langle\tilde{\sigma}_{22}\rangle\gamma_{12} + 2\langle\tilde{\sigma}_{33}\rangle\gamma_{23} + 2\langle\tilde{\sigma}_{44}\rangle\gamma_{24} & 0 & \langle\tilde{\sigma}_{23}\rangle\gamma_{12} & 0 \\ 0 & 2\langle\tilde{\sigma}_{22}\rangle(\gamma_{14}+\gamma_{24}) + 2\langle\tilde{\sigma}_{33}\rangle\gamma_{23} + 2\langle\tilde{\sigma}_{44}\rangle\gamma_{24} & 0 & 2\langle\tilde{\sigma}_{23}\rangle(\gamma_{14}+\gamma_{24}) \\ \langle\tilde{\sigma}_{32}\rangle\gamma_{12} & 0 & 0 & 0 \\ 0 & 2\langle\tilde{\sigma}_{32}\rangle(\gamma_{14}+\gamma_{24}) & 0 & 2\langle\tilde{\sigma}_{33}\rangle(\gamma_{14}+\gamma_{24}) \end{pmatrix}, \tag{A15}$$

$$D_{\alpha_i^\dagger,\alpha_j} = \begin{pmatrix} 2\langle\tilde{\sigma}_{11}\rangle\gamma_{12} + 2\langle\tilde{\sigma}_{33}\rangle\gamma_{13} + 2\langle\tilde{\sigma}_{44}\rangle\gamma_{14} & \langle\tilde{\sigma}_{14}\rangle\gamma_{12} & 0 & 0 \\ \langle\tilde{\sigma}_{41}\rangle\gamma_{12} & 0 & 0 & 0 \\ 0 & 0 & 2\langle\tilde{\sigma}_{11}\rangle(\gamma_{13}+\gamma_{23}) + 2\langle\sigma_{33}\rangle\gamma_{13} + 2\langle\tilde{\sigma}_{44}\rangle\gamma_{14} & 2\langle\tilde{\sigma}_{14}\rangle(\gamma_{13}+\gamma_{23}) \\ 0 & 0 & 2\langle\tilde{\sigma}_{41}\rangle(\gamma_{13}+\gamma_{23}) & 2\langle\tilde{\sigma}_{44}\rangle(\gamma_{13}+\gamma_{23}) \end{pmatrix}, \tag{A16}$$

with α_i denoting 21, 24, 31, and 34 and $\alpha_i^\dagger$ denoting 12, 42, 13, and 43. The expectation values of atomic operators in Eqs. (A15) and (A16) are given by

$$\langle\tilde{\sigma}_{11}\rangle = \frac{2\gamma_{13}|\Omega_c(z)|^2[4(\gamma_{14}+\gamma_{24})^2 + 4\Delta_p^2 + |\Omega_p(z)|^2]}{T}, \tag{A17}$$

$$\langle\tilde{\sigma}_{22}\rangle = \frac{2\gamma_{24}[4(\gamma_{13}+\gamma_{23})^2 + |\Omega_c(z)|^2]|\Omega_p(z)|^2}{T}, \tag{A18}$$

$$\langle\tilde{\sigma}_{33}\rangle = \frac{2\gamma_{24}|\Omega_c(z)\Omega_p(z)|^2}{T}, \tag{A19}$$

$$\langle\tilde{\sigma}_{44}\rangle = \frac{2\gamma_{13}|\Omega_c(z)\Omega_p(z)|^2}{T}, \tag{A20}$$

$$\langle\tilde{\sigma}_{14}\rangle = -\frac{4\gamma_{13}[\Delta_p - i(\gamma_{14}+\gamma_{24})]|\Omega_c(z)|^2\Omega_p(z)}{T}, \tag{A21}$$

$$\langle\tilde{\sigma}_{23}\rangle = \frac{i4(\gamma_{13}+\gamma_{23})\gamma_{24}\Omega_c(z)|\Omega_p(z)|^2}{T}, \tag{A22}$$

where

$$T = 4\gamma_{13}[2(\gamma_{14}+\gamma_{24})^2 + 2\Delta_p^2 + \Omega_p(z)|^2]|\Omega_c(z)|^2 + 4\gamma_{24}[2(\gamma_{13}+\gamma_{23})^2 + |\Omega_c(z)|^2]|\Omega_p(z)|^2. \tag{A23}$$

The diffusion matrix in Eq. (A15) contains only excited-state populations; it thus will be very small when the pump is weak and far detuned. In this case, its contribution to the Glauber function will be small.

[1] S. L. Braunstein, and P. van Loock, Quantum information with continuous variables, Rev. Mod. Phys. **77**, 513 (2005).

[2] N. Gisin, G. Ribordy, W. Tittel, and H. Zbinden, Quantum cryptography, Rev. Mod. Phys. **74**, 145 (2002).

[3] Z. Y. Ou and Y. J. Lu, Cavity Enhanced Spontaneous Parametric Down-Conversion for the Prolongation of Correlation Time Between Conjugate Photons, Phys. Rev. Lett. **83**, 2556 (1999).

[4] C. E. Kuklewicz, F. N. C. Wong, and J. H. Shapiro, Time-Bin-Modulated Biphotons from Cavity-Enhanced Down-Conversion, Phys. Rev. Lett. **97**, 223601 (2006).

[5] X.-H. Bao, Y. Qian, J. Yang, H. Zhang, Z.-B. Chen, T. Yang, and J.-W. Pan, Generation of Narrow-Band Polarization-Entangled Photon Pairs for Atomic Quantum Memories, Phys. Rev. Lett. **101**, 190501 (2008).

[6] C.-S. Chuu and S. E. Harris, Ultrabright backward-wave biphoton source, Phys. Rev. A **83**, 061803(R) (2011).

[7] C.-S. Chuu, G. Y. Yin, and S. E. Harris, A miniature ultrabright source of temporally long, narrowband biphotons, Appl. Phys. Lett. **101**, 051108 (2012).

[8] V. Balic, D. A. Braje, P. Kolchin, G. Y. Yin, and S. E. Harris, Generation of Paired Photons with Controllable Waveforms, Phys. Rev. Lett. **94**, 183601 (2005).

[9] S. Du, J. Wen, M. H. Rubin, and G. Y. Yin, Four-Wave Mixing and Biphoton Generation in a Two-Level System, Phys. Rev. Lett. **98**, 053601 (2007).

[10] S. Du, P. Kolchin, C. Belthangady, G. Y. Yin, and S. E. Harris, Subnatural Linewidth Biphotons with Controllable Temporal Length, Phys. Rev. Lett. **100**, 183603 (2008).

[11] B. Srivathsan, G. K. Gulati, B. Chng, G. Maslennikov, D. Matsukevich, and C. Kurtsiefer, Narrow Band Source of Transform-Limited Photon Pairs via Four-Wave Mixing in a Cold Atomic Ensemble, Phys. Rev. Lett. **111**, 123602 (2013).

[12] L. Zhao, X. Xian, C. Liu, Y. Sun, M. M. T. Loy, and S. Du, Photon pairs with coherence time exceeding 1μs, Optica **1**, 84 (2014).

[13] P. Kolchin, C. Belthangady, S. Du, G. Y. Yin, and S. E. Harris, Electro-Optic Modulation of Single Photons, Phys. Rev. Lett. **101**, 103601 (2008).

[14] S. Zhang, J. F. Chen, C. Liu, M. M. T. Loy, G. K. L. Wong, and S. Du, Optical Precursor of a Single Photon, Phys. Rev. Lett. **106**, 243602 (2011).

[15] S. Zhou, S. Zhang, C. Liu, J. F. Chen, J. Wen, M. M. T. Loy, G. K. L. Wong, and S. Du, Optimal storage and retrieval of single-photon waveforms, Opt. Express **20**, 24124 (2012).

[16] S. Zhang, C. Liu, S. Zhou, C.-S. Chuu, M. M. T. Loy, and S. Du, Coherent Control of Single-Photon Absorption and Reemission in a Two-Level Atomic Ensemble, Phys. Rev. Lett. **109**, 263601 (2012).

[17] C. Liu, S. Zhang, L. Zhao, P. Chen, C.-H. Fung, H. Chau, M. Loy, and S. Du, Differential-phase-shift quantum key distribution using heralded narrow-band single photons, Opt. Express **21**, 9505 (2013).

[18] A. Valencia, A. Cere, X. Shi, G. Molina-Terriza, and J. P. Torres, Shaping the Waveform of Entangled Photons, Phys. Rev. Lett. **99**, 243601 (2007).

[19] S. Du, J. Wen, and C. Belthangady, Temporally shaping biphoton wave packets with periodically modulated driving fields, Phys. Rev. A **79**, 043811 (2009).

[20] J. F. Chen, S. Zhang, H. Yan, M. M. T. Loy, G. K. L. Wong, and S. Du, Shaping Biphoton Temporal Waveforms with Modulated Classical Fields, Phys. Rev. Lett. **104**, 183604 (2010).

[21] J. M. Wen and M. H. Rubin, Transverse effects in paired-photon generation via an electromagnetically induced transparency medium. I. Perturbation theory, Phys. Rev. A **74**, 023808 (2006).

[22] J. M. Wen, S. Du, and M. H. Rubin, Biphoton generation in a two-level atomic ensemble, Phys. Rev. A **75**, 033809 (2007).

[23] J. M. Wen, S. Du, and M. H. Rubin, Spontaneous parametric down-conversion in a three-level system, Phys. Rev. A **76**, 013825 (2007).

[24] J. M. Wen, S. Du, Y. Zhang, M. Xiao, and M. H. Rubin, Nonclassical light generation via a four-level inverted-Y system, Phys. Rev. A **77**, 033816 (2008).

[25] S. Du, J. M. Wen, and M. H. Rubin, Narrowband biphoton generation near atomic resonance, J. Opt. Soc. Am. **B25**, C98 (2008).

[26] P. Kolchin, Electromagnetically-induced-transparency-based paired photon generation, Phys. Rev. A **75**, 033814 (2007).

[27] C. H. R. Ooi, Q. Sun, M. S. Zubairy, and M. O. Scully, Correlation of photon pairs from the double Raman amplifier: Generalized analytical quantum Langevin theory, Phys. Rev. A **75**, 013820 (2007).

[28] J. M. Wen and M. H. Rubin, Transverse effects in paired-photon generation via an electromagnetically induced transparency medium. II. Beyond perturbation theory, Phys. Rev. A **74**, 023809 (2006).

[29] D. A. Braje, V. Balic, S. Goda, G. Y. Yin, and S. E. Harris, Frequency Mixing Using Electromagnetically Induced Transparency in Cold Atoms, Phys. Rev. Lett. **93**, 183601 (2004).

[30] S. E. Harris, Electromagnetically induced transparency, Phys. Today **50**, 36 (1997).

[31] M. Fleischhauer, A. Imamoglu, and J. P. Manarangos, Electromagnetically induced transparency: Optics in coherent media, Rev. Mod. Phys. **77**, 633 (2005).

[32] M. H. Rubin, D. N. Klyshko, Y. H. Shih, and A. V. Sergienko, Theory of two-photon entanglement in type-II optical parametric down-conversion, Phys. Rev. A. **50**, 5122 (1994).

[33] J. F. Clauser, Experimental distinction between the quantum and classical field-theoretic predictions for the photoelectric effect, Phys. Rev. D **9**, 853 (1974).

[34] P. Grangier, G. Roger, and A. Aspect, Experimental evidence for a photon anticorrelation effect on a beam splitter: A new light on single-photon interferences, Europhys. Lett. **1**, 173 (1986).

[35] L. Zhao, X. Guo, Y. Sun, Y. Su, M. M. T. Loy, and S. Du, Shaping the Biphoton Temporal Waveform with Spatial Light Modulation, Phys. Rev. Lett. **115**, 193601 (2015).